2024-05-01

Microwave Emission Model Parameter Tuning For Surface Soil Moisture Retrieval Using Uav-Mounted Dual Polarization L-Band Radiometer

Santiago Hoyos Echeverri
University of Texas at El Paso

Recommended Citation

Hoyos Echeverri, Santiago, "Microwave Emission Model Parameter Tuning For Surface Soil Moisture Retrieval Using Uav-Mounted Dual Polarization L-Band Radiometer" (2024). *Open Access Theses & Dissertations*. 4107.
https://scholarworks.utep.edu/open_etd/4107

MICROWAVE EMISSION MODEL PARAMETER TUNING FOR SURFACE SOIL MOISTURE RETRIEVAL USING UAV-MOUNTED DUAL POLARIZATION L-BAND RADIOMETER

SANTIAGO HOYOS ECHEVERRI

Master's Program in Environmental Science

APPROVED:

Hernan A. Moreno, Ph.D., Chair

Jose M. Hurtado, Ph.D.

Derek Houtz, Ph.D.

Stephen L. Crites, Jr., Ph.D.
Dean of the Graduate School

To my dear family and friends,

whose support and love knows no boundaries.

Even far, far, away, your encouragement

has been source of strength.

In loving memory of

Martha & Magnus.

MICROWAVE EMISSION MODEL PARAMETER TUNING FOR SURFACE SOIL MOISTURE RETRIEVAL USING UAV-MOUNTED DUAL POLARIZATION L-BAND RADIOMETER

by

SANTIAGO HOYOS ECHEVERRI

THESIS

Presented to the Faculty of the Graduate School of
The University of Texas at El Paso
in Partial Fulfillment
of the Requirements
for the Degree of

MASTER OF SCIENCE

Department of Earth, Environmental and Resource Sciences
THE UNIVERSITY OF TEXAS AT EL PASO
May 2024

Acknowledgements

Completing this master's thesis was a collaborative effort, with individuals and institutions playing crucial roles. In particular, Hernan Moreno and Derek Houtz deserve special recognition for their unique contributions. Their guidance and support were invaluable and instrumental in shaping the direction of this research and navigating its complexities. Deep gratitude is extended to Andres Monsalve, Jorge Mayo, Stephanie Marquez, Rosa España, Jayanga Samarasinghe, and Isabela Suaza for their teachings and insights that enriched the understanding of geospatial sciences. Their dedication to knowledge sharing and fostering intellectual growth has been inspiring. Furthermore, appreciation is expressed towards Jose Hurtado, Marguerite Mauritz-Tozer, Lixin Jin, and Mark Engle for their invaluable advice and feedback, which significantly contributed to refining this thesis and ensuring its academic rigor. Special acknowledgment is reserved for Ryan Cruz, Stephanie Marquez, Zachary Camarillo, Jorge Mayo, Betul Aslantas, Valentina Sanchez, Carley Oliver, and Marissa Nuñez, whose support in the field was indispensable. Their assistance was essential in collecting the necessary data and enriching the research process. Additionally, special mention to Tristan, Nayla, Nuria, Fernando, Ben Brunner, Gail Arnold, and David Young, whose camaraderie and support made the journey through graduate school not only memorable and enriching but also comforting. Their encouragement and friendship have been more than just a source of strength and motivation; they have been a lifeline. Lastly, sincere gratitude is extended to The University of El Paso, GeosenSE, The Organization of American States, Laura Alvarez, James Lubicki, Philip Goodell, and Craig Tweedie for their unwavering support and provision of resources. Their commitment to academic excellence and research advancement has been foundational in this academic journey.

Abstract

Surface soil moisture retrieval from L-band brightness temperature has been developed for the past decades due to multiple beneficial characteristics of 1-2 GHz frequency bands for remote sensing of the environment. Numerous microwave emission models have been proposed for tower and satellite-based operations with successful retrieval of surface soil moisture and vegetation water content. As a result of the development of cost-effective and low-mass microwave L-band radiometers such as the Portable L-band Radiometer (PoLRa), surface soil moisture surveying traditionally developed by satellite missions SMOS and SMAP can now be developed at local scales, bringing these operations to commercial small unmanned aerial systems (sUAS) providing high detail resolution retrievals at low elevation (7 m or lower depending on canopy height). Due to its cost and limited access, low-altitude, sub-orbital L-band dual polarization radiometry operations for soil moisture retrieval still need further exploration. This study used an sUAS-mounted L-band radiometer and a multispectral camera to model surface soil moisture over irrigated alfalfa cropland in New Mexico's Rio Grande Valley. This setting allowed varying soil and vegetation moisture conditions, validating with commercial soil moisture probes. This work compared dual and single polarization algorithms using the single scattering Tau-Omega (τ-ω) model with a conventional dielectric mixing scheme, a semi-empirical HQN roughness model and NDVI derived τ to retrieve soil moisture. The calibrated high resolution (4.5 m footprint) dual-polarization retrievals presented superior accuracy for estimating ground truth moisture under dry conditions with RMSE values between 0.03-0.054 cm^3/cm^3, and 0.068-0.115 cm^3/cm^3 after irrigation. Horizontal polarization single retrievals performed favorably against vertical. This study identified improvements for commercial applications and highlighted the potential of sUAS to achieve competent soil moisture and vegetation water content retrievals in semi-arid lands for low canopy land covers.

Table of Contents

Page

Appendix

List of Tables

List of Figures

List of Abbreviations

Abbreviation	**Meaning**
DCA	Dual Channel Algorithm
DEM	Digital Elevation Model
EC	Electrical Conductivity
EM	Microwave Emission Models
EMI	Electromagnetic Interference
FAA	Federal Aviation Administration
GPS	Global Positioning System
JER	Jornada Experimental Range
L-MEB	L-band Microwave Emission of the Biosphere
LiDAR	Light Detection and Ranging
NIR	Near-infrared
NDVI	Normalized Difference Vegetation Index
PI	Principal Investigator
PoLRa	Portable L-band Radiometer
RGB	Red, Green and Blue
SfM	Structure from Motion
SMAP	Soil Moisture Active Passive satellite
SMOS	Soil Moisture and Ocean Salinity satellite
sUAS	Small Unmanned Aerial System
TO	Tau-omega
UAS	Unmanned Aerial System
UAV	Unmanned Aerial Vehicle
UTEP	The University of Texas at El Paso
VWC	Vegetation Water Content
VTOL	Vertical Take-off and Landing

Chapter 1

Introduction

Surface soil moisture is critical for understanding soil characteristics, biogeochemical cycles and land-atmosphere interactions, soil suitability for human activities, and floods and droughts. Several measuring techniques have been proposed for scales ranging from plot to continental scale, but the highly intricate spatial variability requires complex instruments and methodologies (Susha et al., 2014). Within this context, remote sensing has advantages in covering vast areas, reducing manual labor, and accessing difficult locations.

Microwave remote sensing is a valuable method for measuring environmental and object characteristics using microwaves (Karthikeyan et al., 2017a). This technique has numerous applications in meteorology, hydrology, forestry, agriculture, and oceanography (Schwank et al., 2018). Its capability to sense through clouds, smoke, and atmospheric interference makes it significant for weather forecasting, climate monitoring, and environmental research (Calla et al., 2008). Moreover, it can detect features not visible to optical sensors, including atmospheric water vapor, sea surface salinity (Bao et al., 2019), and soil moisture. These technologies use microwave radiometers or radars on tower, satellite, or aircraft systems that measure the intensity of the microwaves emitted or reflected by the Earth's surface (Karthikeyan et al., 2017b). The collected data is used to create imagery and other products that can be analyzed to extract information about the observed objects and environment. L-band radiometers have been identified as a promising approach for soil moisture retrievals due to their advantageous remote sensing characteristics in the 1-2 GHz frequency range relative to higher frequency bands like X-band and C-band. L-band frequencies can penetrate deeper into the soil (up to 5 cm) and are sensitive to soil moisture for vegetation water contents up to 5 kg/m^2 while protected against electromagnetic interference (EMI) by international law (Entekhabi, Njoku, et al., 2010). Unlike radars, L-band radiometers are relatively insensitive to surface roughness and vegetation scattering and offer better performance, though at the cost of coarser spatial resolution (Entekhabi, Njoku, et al., 2010).

Numerous Microwave Emission Models (EM) exist for retrieving various environmental variables using L-band's brightness temperature (T_b) data (Karthikeyan et al., 2017a; Schwank et al., 2018). These models have been successfully applied to different remote sensing systems for retrieving surface soil moisture, ice wetness, vegetation optical depth, and vegetation water content (Das et al., 2019; Houtz et al., 2021; Konings et al., 2016; Srivastava, 2017). Two widely used EM models are the tau-omega (TO) and the L-band Microwave Emission of the Biosphere (L-MEB), both based on the EM model by Mo et al. (1982) (Chan et al., 2012; Wigneron et al., 2007). These models are incorporated into the retrieval algorithms of Soil Moisture and Ocean Salinity (SMOS) and Soil Moisture Active Passive (SMAP) missions, respectively. The TO EM model describes the signal measured in terms of soil, vegetation, atmosphere, and sky emissions. This study utilized the simplest version of the model, which only includes soil and vegetation components used by the SMOS and SMAP missions. The HQN roughness model initially developed by Wang and Choudhury (1981) that models surface roughness effects is incorporated, with modifications made to account for polarization mixing effects (Q), angular effects on reflectivity (N), and intensity of roughness effects (H). Additionally, the model includes a dielectric mixing model for precise soil moisture retrievals. Since the 1980s, numerous studies have been conducted to understand and model the electrical properties of soil, with Topp et al. (1980) being one of the key authors in this field. Other models have been proposed for different soil properties and instruments, such as those presented by Karthikeyan et al. (2017a), Matzler and Murk (2010), and Srivastava et al. (2015).

In recent years, technological advancements have enabled soil moisture measurements at local scales using drones equipped with low-mass L-band radiometers such as The PoLRa: Portable L-band Radiometer (Houtz et al., 2020a). The PoLRa provides higher precision and maneuverability compared to previous fixed-wing ultra-light radiometers (Acevo-Herrera et al., 2009; Dai et al., 2016; Dai et al., 2021; McIntyre & Gasiewski, 2007; Valencia et al., 2008). This has opened up new possibilities for high-resolution soil moisture mapping with spatial resolution under 6 m, depending on canopy height. However, using L-band radiometry for ground-based soil moisture retrieval in arid regions still needs to be explored, and further research is needed to realize its full potential.

This Master's thesis tested soil moisture retrieval models that accurately estimated surface soil moisture (up to 12 cm depth) using L-band T_b readings in semi-desert soils under varying humidity conditions with short crops and irrigation schedules. The models included the assimilation of vegetation-related reflectances from multi-spectral cameras to enhance the retrievals. The study used dual-polarization L-band data from multiple aerial missions over a cultivated field in the Rio Grande Valley near El Paso (TX) - Las Cruces (NM) corridor. Surface soil moisture retrievals were validated with volumetric soil moisture measurements and compared with 12 cm depth in-situ readings. Additionally, the study included the retrieval of Vegetation Optical Depth (τ) and Vegetation Volumetric Water (VWC) content from NDVI, which are linearly correlated. The parameterization schemes that better captured the spatial variability of soil moisture were recommended based on the model validation results.

Chapter 2

Research Questions, Hypothesis, and Objectives.

2.1 Science Questions

1. How can the retrieval of high-resolution soil moisture from Unmanned Aerial System (UAS) L-band brightness temperature readings be improved so that an operative model accurately works across various soil moisture conditions?
2. To what extent can incorporating visible and near-infrared bands to L-band radiometry operations enhance our understanding of the spectral emissions of the environment and their relationship with water content in soil and vegetation?

2.2 Hypothesis

The retrieval of high-resolution soil moisture and vegetation water content from Unmanned Aerial System (UAS) L-band brightness temperature readings can be accomplished across varying moisture conditions through the calibration of the Tau-Omega (TO) EM roughness parameters and the utilization of diverse dielectric mixing models. There is a combination of parameters and models that best retrieve soil water content across multiple moisture conditions and perform well beyond training (i.e., validation). Using an optimization scheme within the retrieval algorithm will provide a basis for analyzing the sensitivity of the model performance to each model parameter, allowing to recommend further improvements in retrievals. Additionally, visible and near-infrared information can: (1) Facilitate the understanding of the dual-polarized separation of the T_b and (2) Provide encoded information to the microwave retrievals during certain (or all) soil moisture condition ranges.

2.3 Objectives

The primary objective of this research is to evaluate the efficacy of Unmanned Aerial System (UAS) L-band brightness temperature readings, specifically the tuning of Tau-Omega (TO) EM roughness parameters, in enhancing the retrieval of high-resolution soil moisture under various water content scenarios. Furthermore, this study investigates the potential utility of complementary visible and near-infrared observations in estimating soil moisture. This investigation additionally endeavors to identify areas where various factors may adversely impact the retrievals and evaluate the capacity of UAS-based data to improve such retrievals. Ultimately, the research aims to enhance understanding of water dynamics across spatial and temporal scales.

By achieving these objectives, the study contributes to developing more robust methods for monitoring soil and vegetation water dynamics, improving the utility and reliability of satellite-based products.

Chapter 3

Methods & Data

3.1 Study Area

This study collected soil, meteorological, and multi-spectral data from several aerial missions and ground sampling stations during different soil moisture conditions within a 49 x 49 m area (Figure 3.1) in an irrigated farm in Chamberino, Doña Ana County, New Mexico, U.S.A. The selection of this location was favored for its proximity to the UTEP Campus and the use of a seasonal irrigation scheme. These conditions introduce diverse soil moisture scenarios, presenting an opportunity for various evaluation values.

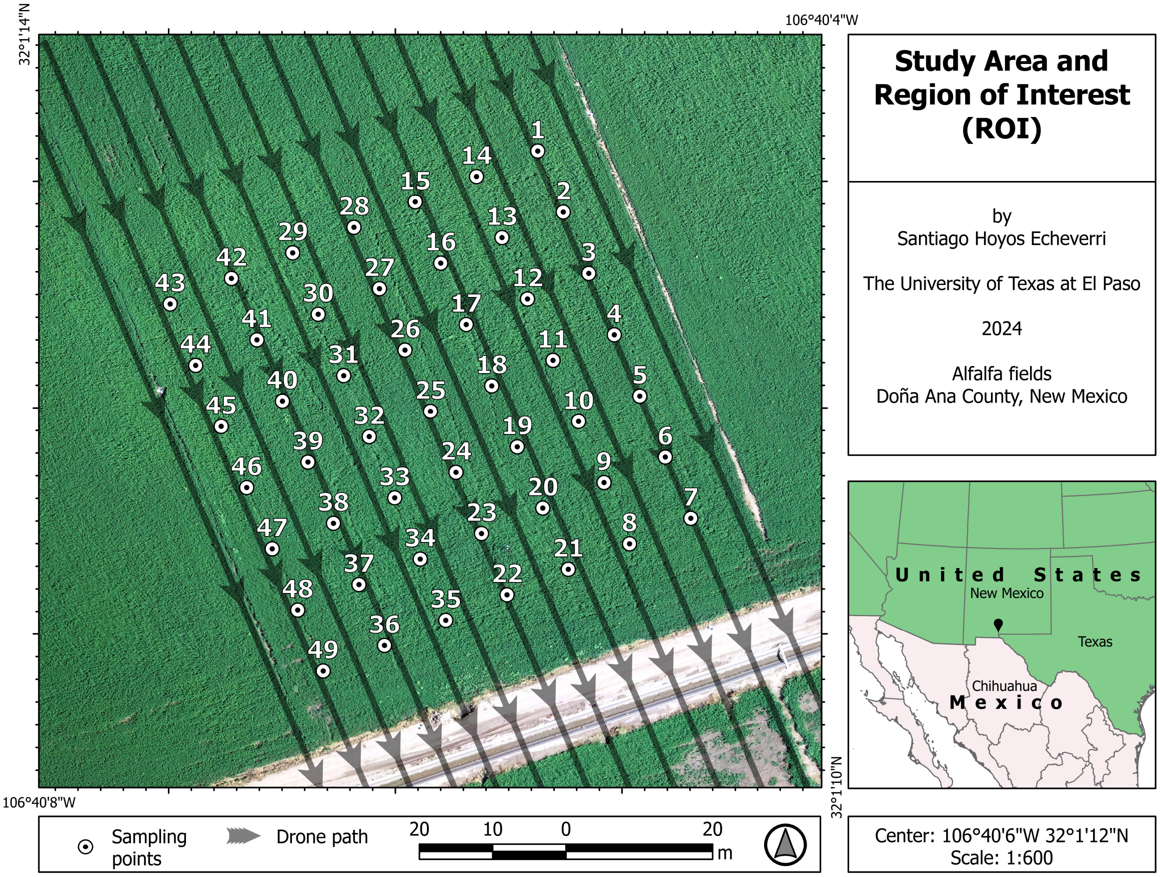

Figure 3.1: Location of the region of interest (ROI), UAS Flight-path lines and probe manual sampling points (1 to 49) at Doña Ana County, New Mexico.

3.2 Instruments

Table 3.1: Specifications of the UAV sensor payloads.

Payloads			
Sensors:	Micasense RedEdge	Portable L-band Radiometer	DJI Phantom 4 Pro V2.0 camera
Frequency/ Wavelength:	Visible (RGB), Red Edge, Near Infrared (NIR)	L-band (1400–1427 MHz)	Visible (RGB)
Observation Mode:	Snap shot 1280 x 960	Dual-linear polarizations (H&V)	Snap shot 5472×3648
Nadir angle:	Nadir	35.5° to 40.5°	Nadir
Beam width:	47.2° H, 35.4° V	36°	84° diagonal
Spatial resolution:	0.08 m (GSD at 120 m)	4.5 m footprint at 7 m AGL	0.03 m (GSD at 120 m)

Table 3.2: Specifications of the moisture sampling equipment.

Moisture sampling	
Sensor:	HydroSense II Handheld Soil
Accuracy:	±3% VWC in mineral soils
Probe:	CS659 (12 cm)

Two UAVs were used to collect airborne data over the irrigated lands; the DJI hexacopter M600 Pro carried the L-band radiometer and the multi-spectral camera separately (one mission each), capturing point data and 5-band images. The quad-copter DJI Phantom 4 Pro V2.0 was used to collect auxiliary RGB pictures. Two portable HSII Campbell scientific loggers with CS659 12cm soil moisture reflectometer probes were used to capture volumetric soil moisture values along the sampling points. Table 3.1 presents the primary payload sensors' specifications in this study and table 3.2 depicts the specifications of the moisture sensors used. Additionally, two project measuring stations were used to monitor 15-minute weather variables (GeoSenSE_Chamberino_22; Ambient Weather WS-2902), and 5-minute system temperatures and soil moisture(GeoSenSE_Chamberino_23; HOBO MX 2303 & MX 2307), to ensure diverse moisture and vegetation scenarios.

3.2.1 DJI Phantom IV and RGB Camera

The Phantom 4 Pro V2.0 is a professional quad-copter developed by DJI with a 1-inch CMOS sensor camera and an 8.8 mm focal length that collects high-quality imagery for filming and surveying. This drone has a maximum wind resistance of 10 m/s and an estimated flight time of 30 minutes. The GPS has a 0.5 m vertical and 1.5 m horizontal accuracy. The system can operate between 0 and 40 Celsius and has a maximum transmission distance of 6 km in the 5.725-5.850 GHz and the 2.400 GHz-2.483 GHz bands.

3.2.2 DJI M600 Pro sUAS

The Matrix 600 Pro is a professional hexa-copter developed by DJI (see Figure 3.2) with a 5.5 kg payload capability that allows high-quality performance for filming and surveying. This drone has a maximum wind resistance of 8 m/s and has an estimated flight time of 26 minutes carrying the PoLRa. The 3-antenna GPS has a 0.5 m vertical and 1.5 m horizontal accuracy. The system can operate between -10 and 40 degrees Celsius and has a maximum transmission distance of 5 km in the 5.725-5.825 GHz and the 2.400 GHz-2.483 GHz bands.

3.2.3 Dual Polarization Microwave Radiometer

The Terrarad Tech Portable L-Band Radiometer (PoLRa) shown in Fig 3.2 (a), is a dual-polarization L-band radiometer that can measure microwave radiation at a frequency of 1.4 GHz. This instrument has a compact, low-mass, stable, simple, and low-power design that enables its deployment on various platforms such as UAVs, vehicles, towers, poles, or buildings. It provides calibrated antenna temperatures with 0.14 K resolution at 1 s integration and 0.6–1.5 K total uncertainty that can be utilized to estimate soil moisture, sea ice thickness, or other environmental processes (Houtz et al., 2020b). The instrument weighs 3.8 kg and is mounted on an M600 Pro hexacopter with a total mass of 13.3 kg. As shown in Fig 3.2 (b), the PoLRa is installed below the drone's main body with an inclination of approximately 40° to achieve an incidence angle between 30° and 50°.

(a) **(b)**

Figure 3.2: Patch array antenna (a) mounted on the tower during sky measurement; (b) mounted on the multi-copter drone during flight measurements. Source: Houtz et al. (2020b).

3.2.4 Multi-spectral Camera

The MicaSense RedEdge-MX is a 12-bit depth multi-spectral camera with five 1.2 MP imagers and a 5.4 mm focal length. It captures imagery with a horizontal and vertical Field of View of 47.2 and 35.4 degrees, respectively. It has five bands: Blue, Green, Red,

Red Edge, and Near-infrared (NIR) with center wavelengths of 475, 560, 668, 717, and 842 nm and bandwidths of 32, 27, 16, 12, and 57 nm. At an altitude of 120 m above the ground level (AGL), this sensor provides a ground sample distance (GSD) of 8 cm.

3.2.5 HS12 Campbell Scientific Soil Moisture Probe

Four (4) HydroSense II handheld soil moisture sensors with a 0.05 % resolution and 3 % accuracy (for electrical conductivity below 6.5 dS/M) were employed for in-situ validations. These sensors use CS659 12 cm dual rod probes. A preliminary evaluation of these probes was done during UTEP Geospatial Sensing and Sampling of the Environment (GeoSenSE) laboratory's Jornada Experimental Range (JER) 2022 campaigns (see 3.3).

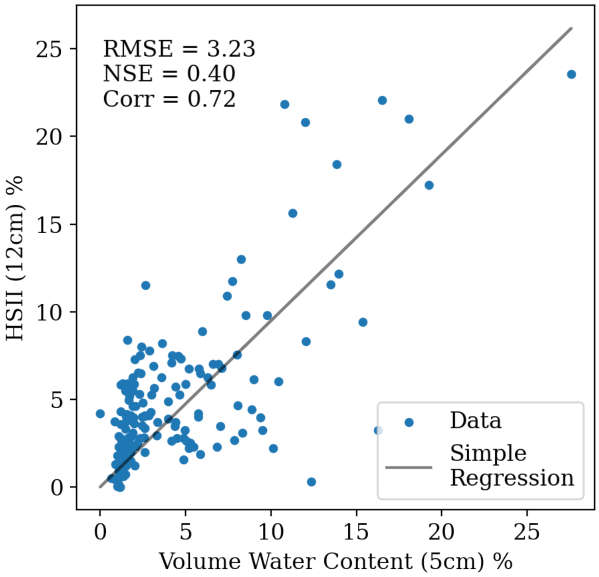

Figure 3.3: Comparison of 5 cm surface soil moisture measurement using gravimetric method against 12 cm HSII readings for seven campaigns conducted during summer 2022 within the USDA Jornada Experimental Range study site 575 led by PI Moreno.

3.3 Data

The sensor setup explained in section 3.2 was used in seven missions between August and October 2023 to obtain airborne data during a wide range of soil moisture values over different stages of alfalfa growth (10-75 cm), spanning from dry to wet soils (7-45% surface soil moisture). 2023 campaign dates were Aug. 16^{th} and 24^{th}; Sept. 4^{th}, 13^{th} and 20^{th}; and Oct. 2^{nd} and 13^{th}. Constant communication was maintained with the land manager regarding visiting the area during various moisture conditions. The mission crew consisted of an FAA Part 107 pilot, an observer, and a ground data collector. The linear pattern shown in 3.1 was designed using the Litchi software, a pioneering UAV way-point mission planning platform, taking into account the payload characteristics to guarantee multiple overlaps with the soil sampling scheme.

The DJI Matrice hexacopter was used to collect horizontal and vertical L-band brightness temperature at 7 m AGL (4.5 m footprint); the point data represents the center of the projected antenna's footprint. The HSII soil moisture probes were used to collect 12-cm volumetric water content measurements at 49 points within the measurement grid (Figure 3.1); a second DJI Matrice hexacopter flight plan was used to collect multi-spectral pictures of the site at 120 m AGL (0.08 m Ground Sampling Distance -GSD). The soil water content measurements occurred before the initial hexacopter mission and between the subsequent multi-spectral imaging mission. Additionally, a weather station and an arrangement of soil sensors were installed to monitor precipitation and irrigation events, soil moisture, and temperature (soil, canopy, and air) before and during the study period.

3.3.1 Temperature Equilibrium

Diurnal air, canopy, and soil temperature curves were developed to determine the most appropriate time frame for the microwave retrievals (see Figure 3.4). 15-minute mean temperature data from July 2023 to October 2023 were analyzed to compute the project's best flying hour and temperature. On average, southern New Mexico's site conditions present thermal equilibrium between canopy and soil around 8:43 am, generating a flying window between 7:33 am and 10:03 am. Therefore, L-band surveying was performed during this time to optimize the TO EM retrievals. The SMAP and SMOS teams use this approach to ascertain the time of day when the atmospheric temperature (T_{atm}), surface temperature (T_c), and soil temperature (T_g) are approximately equivalent.

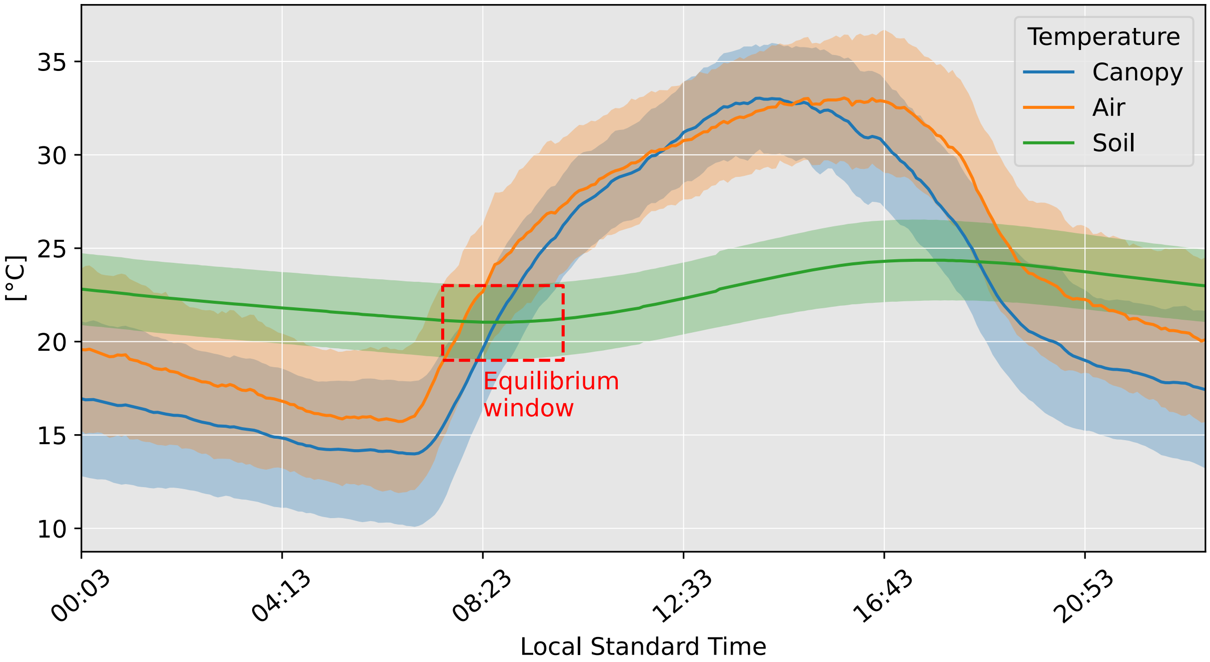

Figure 3.4: Mean diurnal temperature across all media from July to October 2023 at the study site. Data was extracted from installed GeoSenSE_Chamberino22 weather station with air sensors at 2m, canopy at 10cm and soil at 12cm.

3.3.2 Surface Soil Moisture Surveying

A grid of 7 x 7 sampling points within the 49 m x 49 m study area was used to collect surface soil moisture. These probe readings integrated the volumetric water content from the surface to 12 cm depth. At least two stable vertical probe readings were averaged around each sampling point. The insertions were performed to evade cracks in the soil over the dominating soil/vegetation conditions around each location. The mean bulk density of the ROI was 1.5 g/cm^3; as indicated by the manufacturer, the sensor was used in general soil calibration.

3.3.3 Structure from Motion Photogrammetry

Structure from motion (SfM) is a technique that consists of determining the 3D location of an object using 2D images taken from different locations or multiple cameras (Özyeşil et al., 2017). One of the precursors for this set of computer vision algorithms is the 8-point algorithm by Longuet-Higgins (1981). This set of algorithms can be compared to LiDAR products for forestry applications (Iglhaut et al., 2019). The RGB and multi-spectral images were processed using the photogrammetry software Agisoft Metashape, obtaining orthophotos and digital surface models (DSMs) in five bands for every field day.

3.3.4 Multi-spectral Reflectance

During the summer campaigns, multi-spectral imagery was collected using the RedEdge MX system, with 75 % or higher image overlap. The ground sample distance ranged from 8 to 6 cm, achieving higher resolution due to the absence of obstacles. The multi-band imagery was processed using Agisoft Metashape photogrammetric tools based on SfM algorithms with rectification. The images were calibrated using a known reflectance panel before and after each flight and a Downwelling Light Sensor (DLS) to account for light changes during the flight.

Furthermore, the red and infrared reflectances were used to compute the Normalized Difference Vegetation Index (NDVI), a vegetation index widely used to characterize different crop conditions and to estimate the vegetation microwave opacity (NDVI-τ) for Equation 3.3. NDVI was computed using Equation 3.1. This data is expected to correlate with τ retrievals from the dual-channel algorithm explained in section 3.5 and can be used for single moisture retrievals under no electromagnetic interference (EMI) conditions.

$$\mathrm{NDVI} = \frac{(\mathrm{NIR} - \mathrm{Red})}{(\mathrm{NIR} + \mathrm{Red})} \tag{3.1}$$

3.3.5 Microwave L-band Measurements

L-band dual-band brightness temperatures were collected using the PoLRa. These readings were time matched with the sUAS data linearly interpolating inertial measurement unit (IMU) and global positioning system (GPS) unit data to match the radiometer's higher frequency capture, and then projected over the surface using the radiometer's incidence angle. The radiometer faced southeast in all measurements.

3.4 Data Processing and Splitting for Train/Test

Using the L-band data as the parting points in Figure 4.6, soil moisture from Figure 4.5 was spatially matched using the closest probe reading within the footprint of the radiometer (4.5 m diameter) recording the distance value. The NDVI data was spatially joined, grouping all the raster cell values within the footprint and obtaining the mean of this index.

After analyzing in-flight angle variability, data from October 2^{nd} was removed due to its greater variance and unique distribution curve (see Figure 3.5). The radiometer's mean and mode incidence angle were 37.9° and 37.5°, respectively. Angles below 34.8° (5^{th} percentile) or above 41.4° (95^{th} percentile) were excluded to reduce high inclination and potentially biased data. The processed data from August 24^{th} and September 13^{th} were used as validation days due to nadir angle similarities with the SMAP satellite (mean flight angle close to 40°) and their difference in soil moisture, for a total of two out of six days for validation, one moist (on average 0.38 $\mathrm{m}^3/\mathrm{m}^3$) and one dry (on average 0.14 $\mathrm{m}^3/\mathrm{m}^3$). The rest of the days (four out of six) were used for model training and parameter calibration as shown in section 3.6, accounting for a Train/Test split of 67/33.

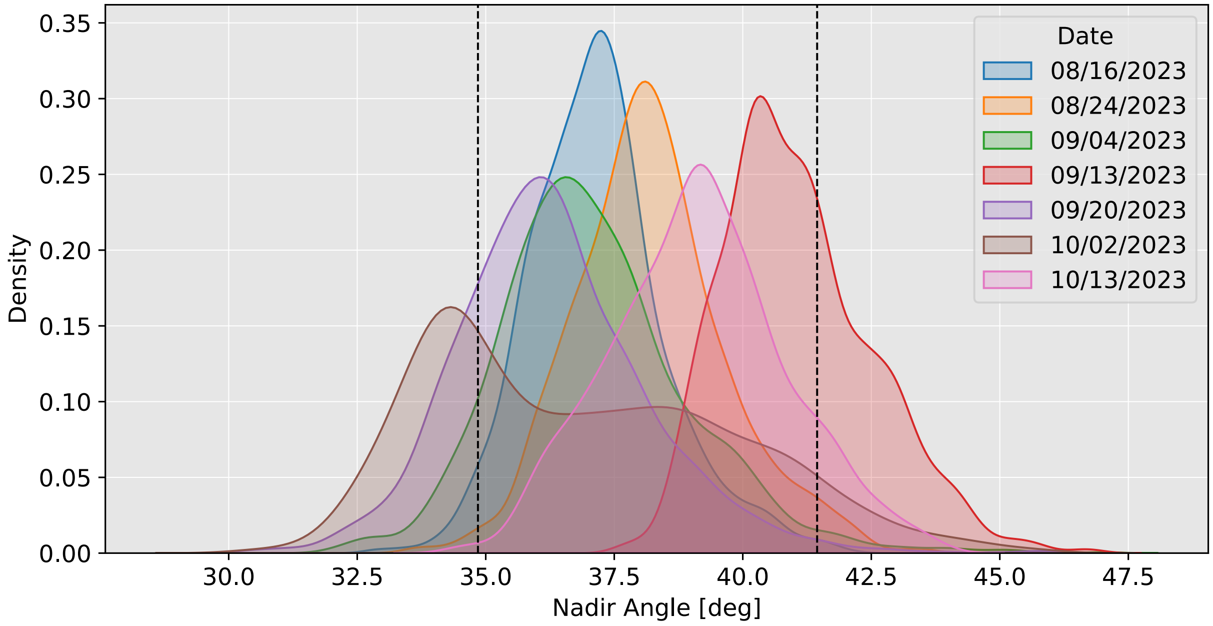

Figure 3.5: Kernel density estimate of the radiometer's incidence angle for each field sampling day.

Following the matching, processing, and splitting of the measurements from the various sources, data post-processing used the retrieval algorithm described next.

3.5 Retrieval Algorithm

This study utilized a dual channel algorithm (based on SMAP's mission Dual Channel Algorithm DCA) to retrieve the top 12 cm surface soil moisture and vegetation opacity from dual-polarization {H,V} brightness temperature and multi-spectral observations using the simplest version of the TO EM model, which only accounts for soil and vegetation components, as utilized by the Soil Moisture and Ocean Salinity (SMOS) and Soil Moisture Active Passive (SMAP) missions (Chan et al., 2012; Wigneron et al., 2007). No other variations of the TO model are considered in this study. Kerr and Njoku (1990), Mo et al. (1982), and Njoku and Entekhabi (1996) developed the fundamentals of this model.

The single scattering Tau Omega model (TO EM) is a radiative transfer framework that simulates the horizontal and vertical polarizations brightness temperature of a vegetated soil surface using two parameters: single scattering albedo (ω) and optical depth (τ) (Park et al., 2020; Shen et al., 2022). The model assumes that multiple scattering is negligible (Shen et al., 2022), and is widely used to estimate soil moisture from microwave remote sensing data (Park et al., 2020; van de Griend et al., 1996).

As stated by Njoku and Entekhabi (1996), the fundamental association between brightness temperature T_B of a thermally radiating object and its actual temperature T is expressed by the equation $T_B = eT$, where e represents the emissivity of the object and T_B is measured in Kelvins. This equation can determine the brightness temperature of the Earth's surface at any particular location with a uniform subsurface temperature profile, given the surface temperature T and emissivity e. As a particular case, for a black body, the emissivity (e) is equal to 1.

Assuming no interference, T_B measured by a UAS-mounted radiometer originates from four different sources: the cosmic background emission, the atmosphere, the vegetation (as a layer), and the ground surface. The reflection and attenuation of these contributions are pictured in Figure 3.4. where TB[1]: brightness temperature (T_B), Sk: sky, atm: atmosphere, c: canopy, and g: ground. According to Chan et al. (2012), the atmospheric contributions (TB_{atm}) and sky brightness (TB_{Sk}) are typically on the order of 2.7 K. Furthermore, the transmissivity of the atmosphere is high, with an optical depth of approximately zero ($\tau_{atm} \approx 0$). As a result, the TO EM model neglects atmospheric and cosmic signals.

---

[1] This study depicts brightness temperature as T_B. The abbreviation TB is used to mantain consistency with the symbology by Kerr et al. (2012) .

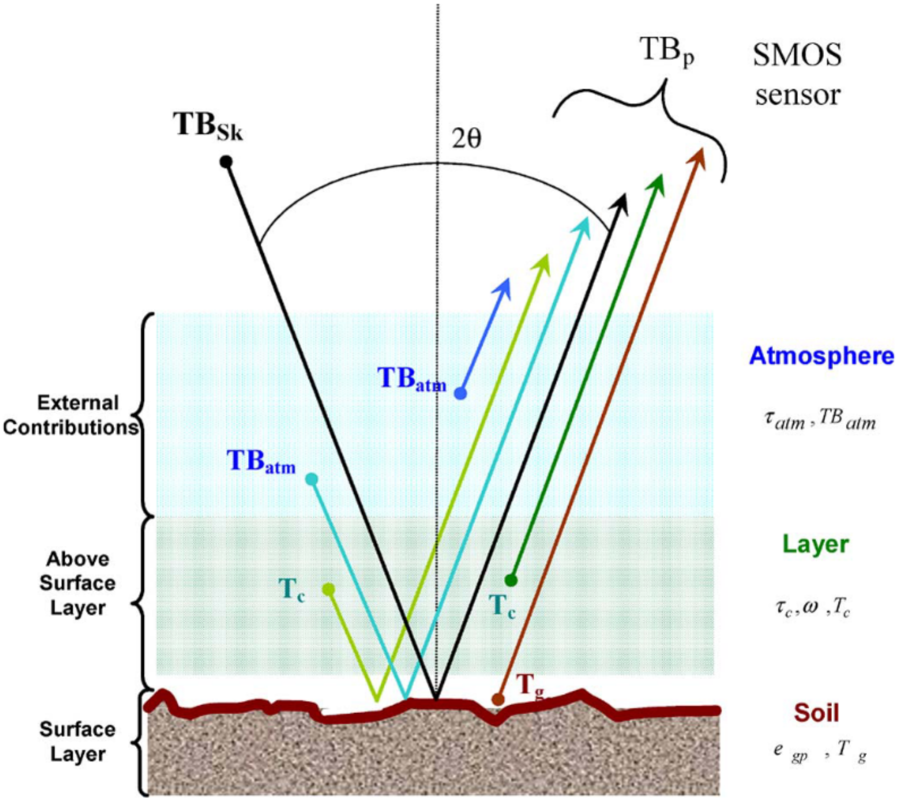

Figure 3.6: Contributions to the observed brightness temperature TB (T_B as depicted in this study) from orbit. Image shows multiple TB beam traces for sky (Sk), atmosphere (atm), canopy (c), and ground (g). Opacity (τ), temperature (T), emissivity (e) and single scatering albedo (ω) are depicted. Source: Kerr et al. (2012).

The TO EM is an approximation of the radiative transfer equation with three terms that account for (i) Emissions from the soil attenuated by the canopy layer, (ii) Direct emissions from the vegetation and (iii) Emissions from the vegetation reflected by the soil. Brightness temperature T_B is expressed as

$$
\begin{aligned}
T_B^p = {} & e_p \cdot T_g \cdot \exp\left(\frac{-\tau}{\cos(\alpha)}\right) \quad \text{(i)} \\
& + (1-\omega)T_c \left(1 - \exp\left(\frac{-\tau}{\cos(\alpha)}\right)\right) \quad \text{(ii)} \\
& + (1-\omega)\cdot(1-e_p)\cdot T_c \left[1 - \exp\left(\frac{-\tau}{\cos(\alpha)}\right)\right] \exp\left(\frac{-\tau}{\cos(\alpha)}\right) \quad \text{(iii)}
\end{aligned}
\tag{3.2}
$$

where:

- ^{p} is the polarization H, V.
- e_p is the emissivity of the soil surface.
- T_g is the effective temperature of the soil.
- τ is the vegetation opacity.
- ω is the single scattering albedo.
- α is the incidence angle.
- T_c is the vegetation temperature.

Conversely, the e_p emissivity of the soil surface can be expressed by Kirchoff's reciprocity theorem in terms of the reflectivity $s_{p,r}$ as $e_p = (1 - s_{p,r})$. This equation shows how the brightness temperature depends on various factors such as soil properties, vegetation characteristics, and sensor geometry. Using such expression for dual polarization {H,V} and some assumptions or empirical relationships makes it possible to invert it and retrieve the soil moisture content SM (see 3.5.2 and 3.5.3) and vegetation opacity τ (see 3.5.1) from T_B measurements.

3.5.1 Vegetation Parameters

Microwave radiation interacts with vegetation through absorption, emission, and scattering processes. A common simplification is representing the vegetation as a homogeneous layer overlying the soil. At lower frequencies, the scattering effects at the interface between air and vegetation and within the vegetation volume are negligible and can be ignored (Njoku & Entekhabi, 1996). The model's vegetation parameters are canopy temperature Tc, isotropic single-scattering albedo ω, and opacity τ. This work used vegetation parameters: $\omega = 0.05$, Stem Factor = 3.5, and b = 0.110. from the SMAP-Sentinel L2 Radar/Radiometer Soil

Moisture (Active/Passive) data products: L2_SM_SP (Das et al., 2019), see Tables A.1-A.3. Dual SM and τ retrievals are possible with the minimization of dual polarization model cost function under no EMI conditions. Nonetheless, this effort only uses single SM retrievals and τ (referred to as NDVI-τ when derived from NDVI) is estimated using the methodology established by the Chan et al. (2013) with UAV multi-spectral data using the equation 3.3

$$\begin{aligned} \mathrm{VWC} = &\left(1.9134 \cdot \mathrm{NDVI}^2 - 0.3215 \cdot \mathrm{NDVI}\right) \\ &+ \text{stem factor} \cdot \frac{\mathrm{NDVI}_{max} - \mathrm{NDVI}_{min}}{1 - \mathrm{NDVI}_{min}} \end{aligned} \tag{3.3}$$

$$\tau = b * \mathrm{VWC}$$

where:

- VWC is the vegetation water content in kg/m^2.
- NDVI is the Normalized difference vegetation index from flights.
- NDVI$_{max}$ is the annual maximum NDVI.
- NDVI$_{min}$ is the annual minimum NDVI, and a global constant value of 0.1 is suggested Chan et al. (2013).
- stem factor is the estimate of the peak amount of water in the stems, taken from Table A.1.
- b is a proportionality value that depends on vegetation structure and microwave frequency.
- τ is the vegetation opacity or optical depth (referred to as NDVI-τ when derived from NDVI).

Vegetation water content (VWC) correlation with opacity was deeply described by Jackson and Schmugge (1991). Finally, canopy temperature Tc is estimated assuming $T_{atm} \approx T_c \approx T_g$, see section 4.2.

3.5.2 Roughness Parameters

The semi-empirical HQN roughness model developed by Wang and Choudhury (1981), best explained by Schwank et al. (2018), which is used in the existing SMOS and SMAP retrieval algorithms, simulates the effect of soil surface-roughness using the following reflectivity equations for both polarizations {H,V}.

$$\begin{aligned} s_{H,r} &= [s_{H,f} \cdot (1 - q_G) + (q_G \cdot s_{V,f})] \cdot e^{-h_G \cdot cos^{n_G^H}(\alpha)} \\ s_{V,r} &= [s_{V,f} \cdot (1 - q_G) + (q_G \cdot s_{H,f})] \cdot e^{-h_G \cdot cos^{n_G^V}(\alpha)} \end{aligned} \tag{3.4}$$

where $s_{V,f}$ and $s_{H,f}$ are the Fresnel reflectivities for the ϵ_G soil permittivity and the α nadir angle defined by the expression

$$s_{V,f} = \left| \frac{(A - B\sqrt{\epsilon_G})}{(A + B\sqrt{\epsilon_G})} \right|^2 \qquad s_{H,f} = \left| \frac{(A\sqrt{\epsilon_G} - B)}{(A\sqrt{\epsilon_G} + B)} \right|^2 \tag{3.5}$$

with $A = \cos(\alpha)$ and $B = \sqrt{1 - \left(\frac{1-A^2}{\epsilon_G}\right)}$.

The HQN parameters were optimized, minimizing the cost function discussed in the next section. The starting HQN values were retrieved from SMAP, SMOS, and literature for similar land covers.

3.5.3 Dielectric mixing model

Soil dielectric models are mathematical equations describing how soil's electric permittivity depends on water content and other factors. There are different types of soil dielectric models. Traditional approaches were proposed by Topp, Mironov, Dobson, Wang and Schmugge, and Hallikainen (Topp et al., 1980; Yayong et al., 2019). More modern works have been proposed by Karthikeyan et al. (2017a), Matzler and Murk (2010), and Srivastava et al. (2015).

The accurate estimation of soil electrical properties is essential for the effectiveness of this methodology. However, complex models demand detailed soil characterization, which may not be feasible in short UAV missions. Therefore, this study adopted Topp's current global reference (see Equation 3.6) as an initial approach due to its efficient simplicity for a broader range of soils without requiring excessive information for general mineral soils.

$$\epsilon_G = 3.03 + 9.3\text{SM} + 146\text{SM}^2 - 76.7\text{SM}^3 \tag{3.6}$$

where ϵ_G is the soil permittivity and SM is the surface soil moisture measured in m^3/m^3.

3.6 Training and Testing

The dual-channel algorithm uses T_B^V and T_B^H observations to retrieve soil moisture by minimizing the loss function (Eq. 3.7). By exploiting the two observations' unique sensitivity to this variable, the algorithm is an effective methodology for estimating surface soil moisture. The loss function is defined as

$$F_{SM} = (T_B^{V\text{observed}} - T_B^{V\text{modeled}})^2 + (T_B^{H\text{observed}} - T_B^{H\text{modeled}})^2 \tag{3.7}$$

Conversely, the single-channel algorithms minimize the function $F_{SM} = (T_B^{\text{observed}} - T_B^{\text{modeled}})^2$ for each polarization.

Where the retrieved SM values are given by $\text{SM} = \arg\min F_{\text{SM}}$. To perform the inversion, an iterative approach was employed to search for the minimum squared difference between simulated brightness temperatures T_B^{modeled} and measured brightness temperatures T_B^{observed}. Iteration boundaries for SM were set using the field data presented in section 3.3.2. The iteration used the L-BFGS-B Algorithm, a limited memory algorithm for bound-constrained optimization developed by Byrd et al. (1995) and Zhu et al. (1997) adapted into the SciPy library. This algorithm is an iterative method that minimizes a nonlinear function (the loss function, in this case) with n variables and different n upper and lower bounds, using a quasi-Newton approach to approximate the Hessian matrix of the loss function using a generalized secant method (Byrd et al., 1995).

The retrieval algorithm was evaluated with the root mean squared error RMSE evaluated as:

$$\text{RMSE} = \sqrt{\frac{1}{n}\sum_{i=1}^{n}\left(\text{SM}_i^{\text{modeled}} - \text{SM}_i^{\text{observed}}\right)^2} \tag{3.8}$$

Two thousand five hundred eighty-three (2,583) combinations of the roughness parameters H, Q, and N were used during the training for dual-band, horizontal, and vertical retrievals. H was evaluated between 0 and 2 in steps of 0.05, Q between 0 and 1 in steps of 0.05, and N was evaluated for $N = 0,\ 1,\ 2$. The calibrated model was selected based on the minimum RMSE obtained during training and validated for Aug. 24^{th} and Sept. 13^{th}, as explained in Section 3.4, obtaining the following results.

Chapter 4

Results

4.1 Field Campaigns Results

Table 4.1 and Figure 4.1 summarize the characteristics of the seven campaigns in terms of significant environmental and sensing variables. While Figure 4.1 illustrates boxplots and average values (crosses) of the distributions of several quantitative variables during each campaign, Table 4.1 averages those values for alternative interpretation. Generally, $T_B^V > T_B^H$, with values between 270 K and 300 K for vertical and 260 K and 290 K for horizontal. Nadir angles were recorded for every L-band measurement, with values between 30° and 45°. Two flooding cycles and two alfalfa cutting cycles were recorded during the campaigns, ensuring diverse moisture and vegetation cover conditions. A 4 K decrease in the soil temperature due to the end of the summer was recorded between the start and the end of the campaigns. Between Aug. 16^{th} and Sept. 20^{th}, rain events were recorded within a week of the flights, which increased vegetation water content. NDVI values rapidly increased with the alfalfa height, reaching means above 0.9 for heights above 19 cm, potentially overestimating NDVI-τ for lower stages of growth.

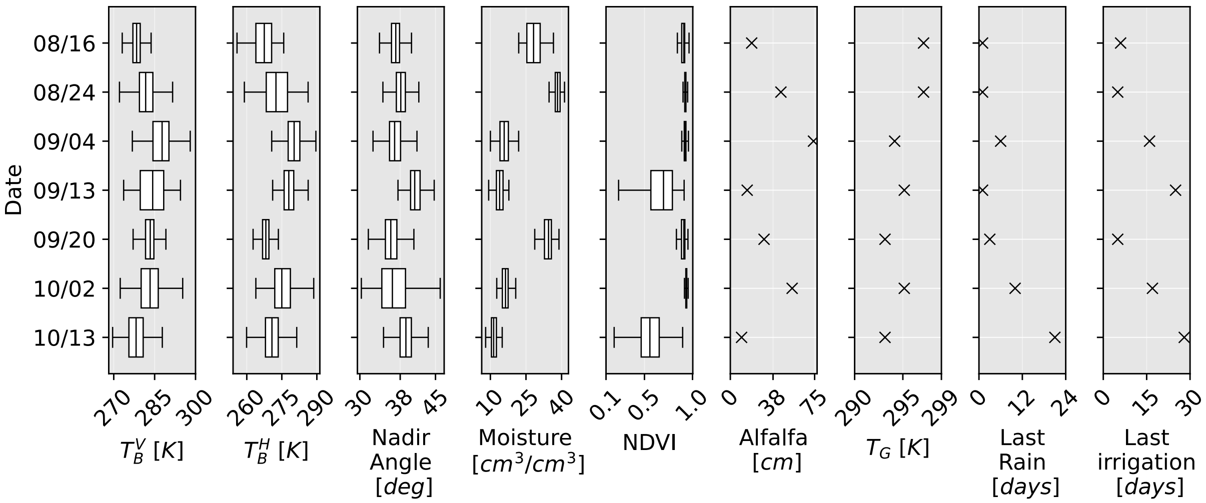

Figure 4.1: Time series of study variables. Vertical L-band brightness temperature (T_B^V), horizontal L-band brightness temperature (T_B^H), inclination of the radiometer (Nadir Angle), HSII volumetric soil moisture (Moisture) and normalized difference vegetation index (NDVI) are represented with box plots for every day. Mean alfalfa height (Alfalfa), mean soil temperature at 12cm (T_G), days from last precipitation (Last Rain) and days from last irrigation (Last irrigation) are represented with scatter plots.

Table 4.1: Study variables and statistics for the seven conducted field campaigns. Mean values are presented for vertical and horizontal L-band brightness temperature (T_B^V and T_B^H), soil temperature (T_g), nadir angle, NDVI, and 12 cm soil moisture. Values are averaged spatially and temporally for each flight.

		Date						
Variable	Units	08/16	08/24	09/04	09/13	09/20	10/02	10/13
T_B^V *	[K]	278.36	281.92	287.31	284.00	283.11	283.17	278.17
T_B^H *	[K]	267.20	272.90	280.17	278.24	268.18	275.64	270.66
Nadir angle *	[°]	37.16	38.20	37.10	41.07	36.27	36.85	39.13
Soil moisture 12cm *	[m^3/m^3]	0.28	0.38	0.16	0.14	0.34	0.16	0.12
NVDI*		0.92	0.93	0.93	0.81	0.92	0.94	0.52
Alfalfa height	[cm]	19	45	74	15	30	55	10
T_g	[K]	297.15	297.15	294.15	295.15	293.15	295.15	293.15
Last rain	[days]	1	1	6	1	3	10	21
Last irrigation	[days]	6	5	16	25	5	17	28

* Spatially averaged variables.

Figure 4.2 portrays the correlation between the study variables when matched spatially and temporally. T_B^V presented a greater positive correlation with NDVI and alfalfa height, while T_B^H had a greater magnitude, negative correlation with surface soil moisture from the HSII probes. The irrigation date had a higher magnitude correlation with most variables, highlighting the importance of the flooding schedule for the vegetation variables and the soil moisture.

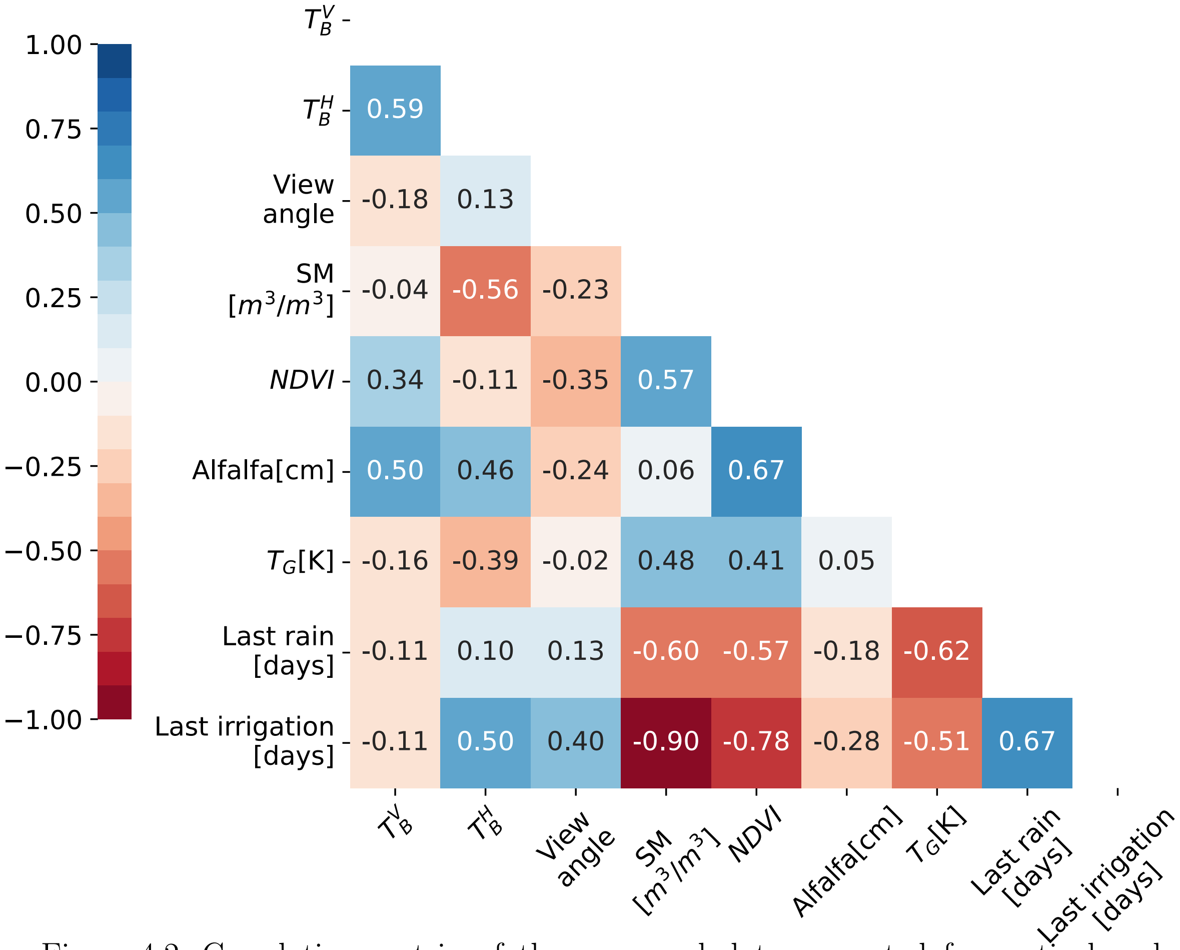

Figure 4.2: Correlation matrix of the processed data presented for vertical and horizontal L-band brightness temperature (T_B^V and T_B^H), nadir angle (View angle), 12cm soil moisture (SM), NDVI, alfalfa height (alfalfa), soil temperature (T_g), days from last precipitation (Last Rain) and days from last irrigation (Last irrigation).

4.1.1 Precipitation and Irrigation Timing and Magnitude

Stations GeoSenSE_Chamberino_22 and GeoSenSE_Chamberino_23, containing a rain gauge and a 12 cm soil moisture probe, respectively, were installed to record the soil moisture variations and the rain events over the paddocks as shown in Figure 4.3. During the study period, the field was irrigated three times and nine rain events were measured. Significant water intercepted by the vegetation was observed during the field dates near rain events. Besides the increase in vegetation water content, most rain events did not significantly affect the volumetric soil moisture measured by the probe.

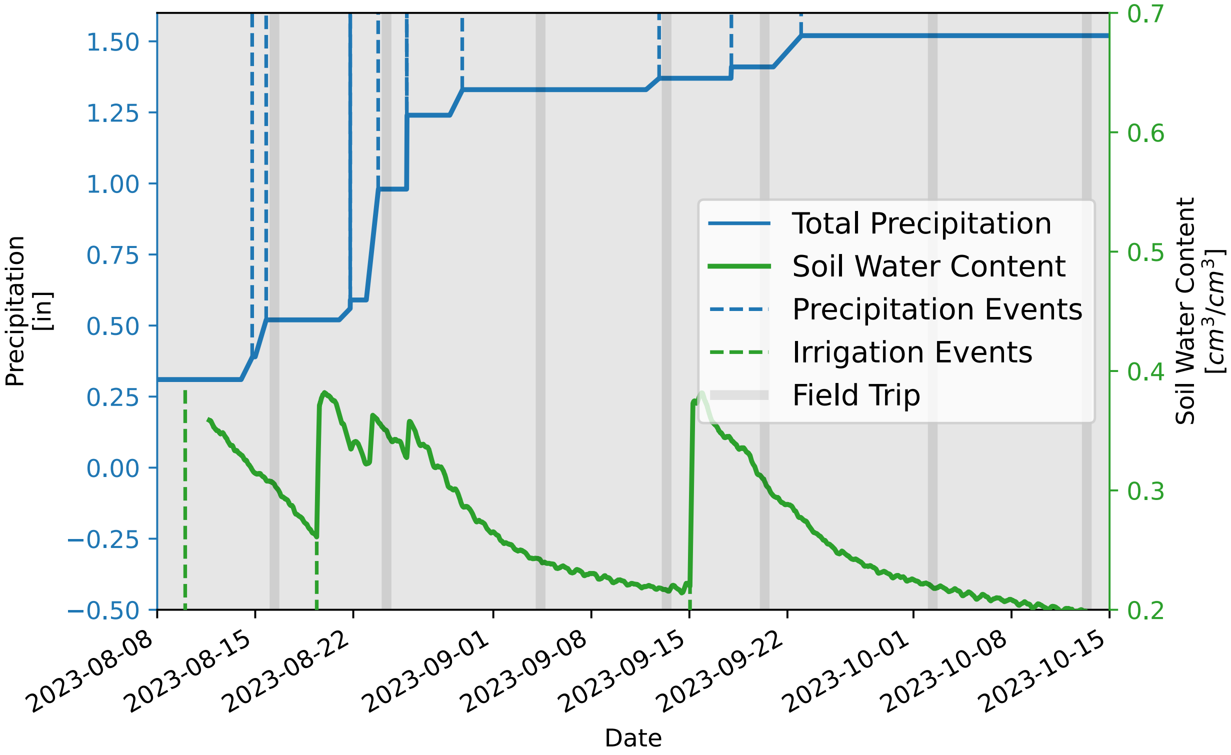

Figure 4.3: Time series of total precipitation (blue), and 12 soil moisture (green) from the installed stations. Field days are symbolized with vertical gray lines. Dotted vertical lines indicate precipitation and irrigation events.

4.1.2 Surface Soil Moisture

The integrated mean 12 cm surface soil moisture was collected each campaign for the 49 grid points following the methodology in Section 3.3.2 with the probes presented in Section 3.2.5. Figure 4.4 illustrates the distribution of each field day's HSII-measured soil moisture values.

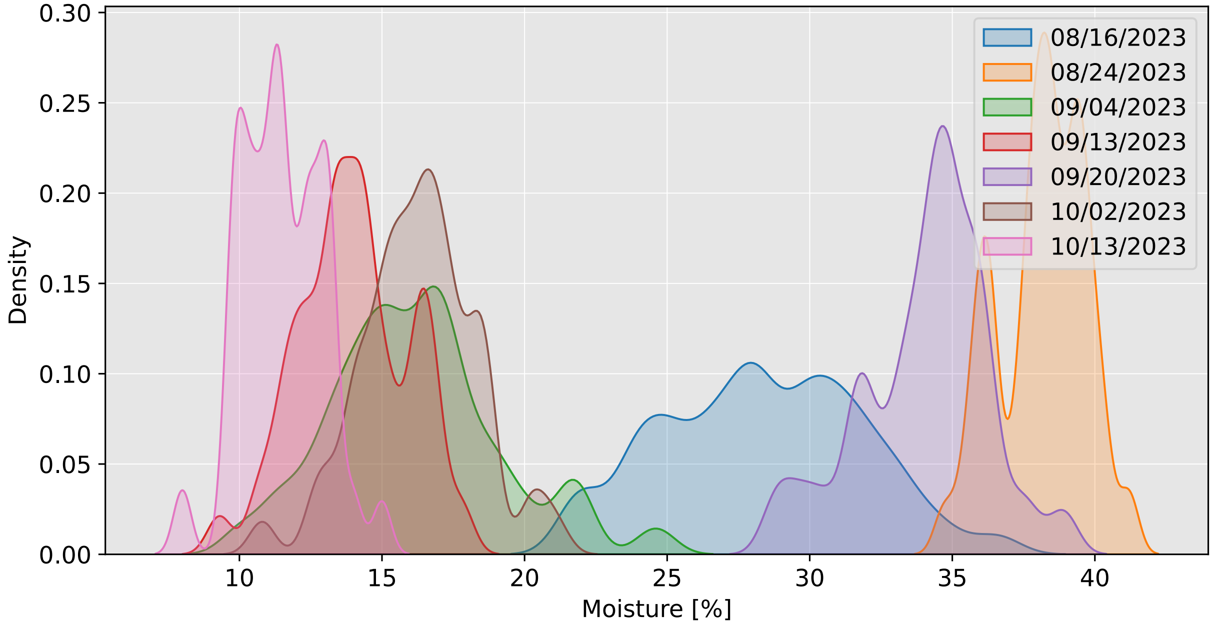

Figure 4.4: Kernel density estimate of the paddock's 12 cm soil moisture for each field sampling day.

The highest moisture recorded was on Aug. 24th with a volumetric content of 0.412 $\mathrm{cm}^3/\mathrm{cm}^3$ only five days after the previous irrigation and one day after the preceding rain event, while the driest measurement was 0.08 $\mathrm{cm}^3/\mathrm{cm}^3$ on Oct. 13th, 28 days after the conducted irrigation. Three campaigns were performed within a week of the field flooding: Aug. 16th, Aug. 24th, and Sept. 20th; two campaigns were performed within three weeks of the irrigation: Sept. 4th and Oct. 2nd; and two campaigns were within five weeks after the last irrigation: Sept. 13th and Oct. 13th. Spatial variations of soil moisture remained low, as expected for a shared paddock with interquantile range IQR < 0.05 m^3/m^3 for all days. Sample points 1 and 14 were greater in moisture than most of their neighbors for most days, signaling a local maximum for all the campaigns at the north extreme of the grid. Points 47, 46, and 44 remained lower than their neighbor points for most days, signaling a local minimum for all the campaigns.

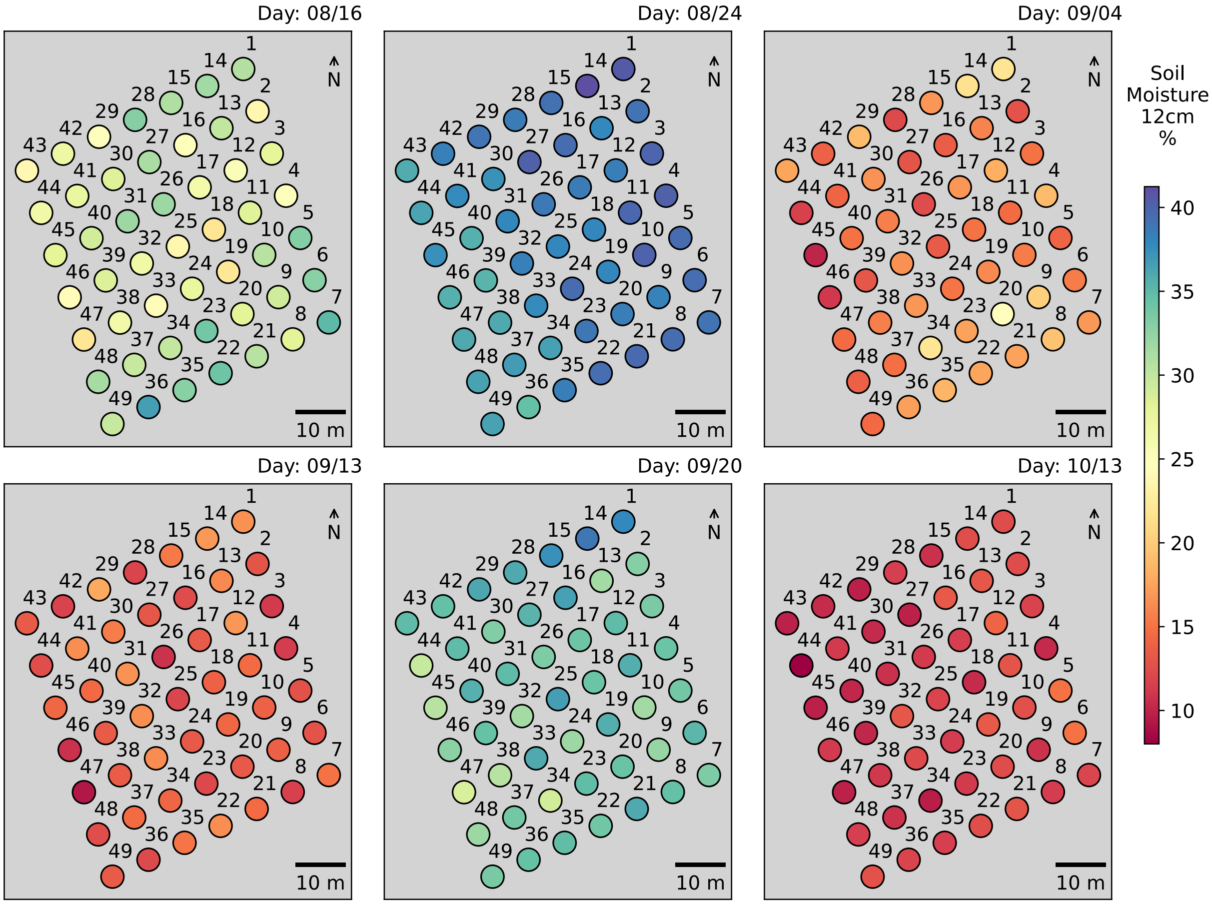

Figure 4.5: Map of the HSII 12cm surface soil moisture measurements for each field campaign of this study.

4.1.3 Multi-spectral and Microwave Sensing

During the campaigns of this study, L-band microwave brightness temperature readings (point data) were obtained using the PoLRa explained in Section 3.2.3. Five band reflectances were also obtained using UAS imagery with the Micasense imager from section 3.2.4. The L-band data was collected in the morning (see section 3.3.1), and the multi-spectral bands were collected between 11 am and 1 pm (LST).

The spatial distribution of the L-band brightness temperatures is presented in figures 4.7 and 4.6, where each point represents the center of the radiometer's projected footprint.

Minimum L-band temperatures were recorded on Aug. 16^{th}, and maximum temperatures were recorded on Aug. 24^{th} for horizontal polarizations, and Aug. 24^{th} and Oct. 13^{th} for the vertical polarizations. Overall, the horizontal polarization temperatures varied more throughout the campaigns than the vertical.

Figure 4.8 presents the arrangement of false color infrared orthophotos. The high GSD (6-8 cm) facilitates the identification of tractor and human tracks on the imagery. Generally, alfalfa grew slower at the bottom row of the grid (points 7, 8, 21, 22, 35, 36 and 49). The methodology in section 3.3.4 was used to compute the NDVI from the red and NIR bands and presented in figure 4.9. The NIR reflectances increased drastically with the growth of the alfalfa, achieving its maximum (0.9) at 19 cm of height.

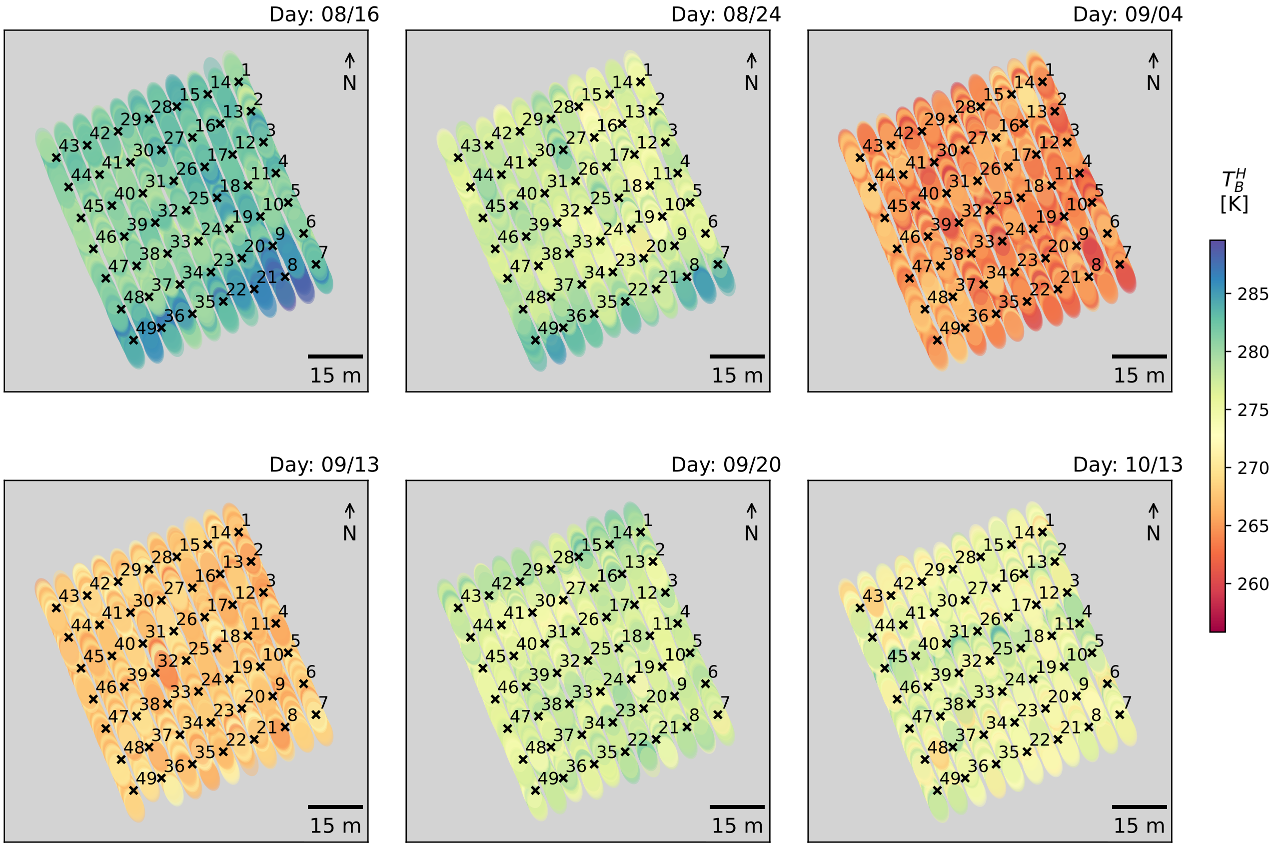

Figure 4.6: Map of L-band horizontal polarization brightness temperature observations. Each point represents the center of the projected radiometer footprint with a 4.5 m diameter.

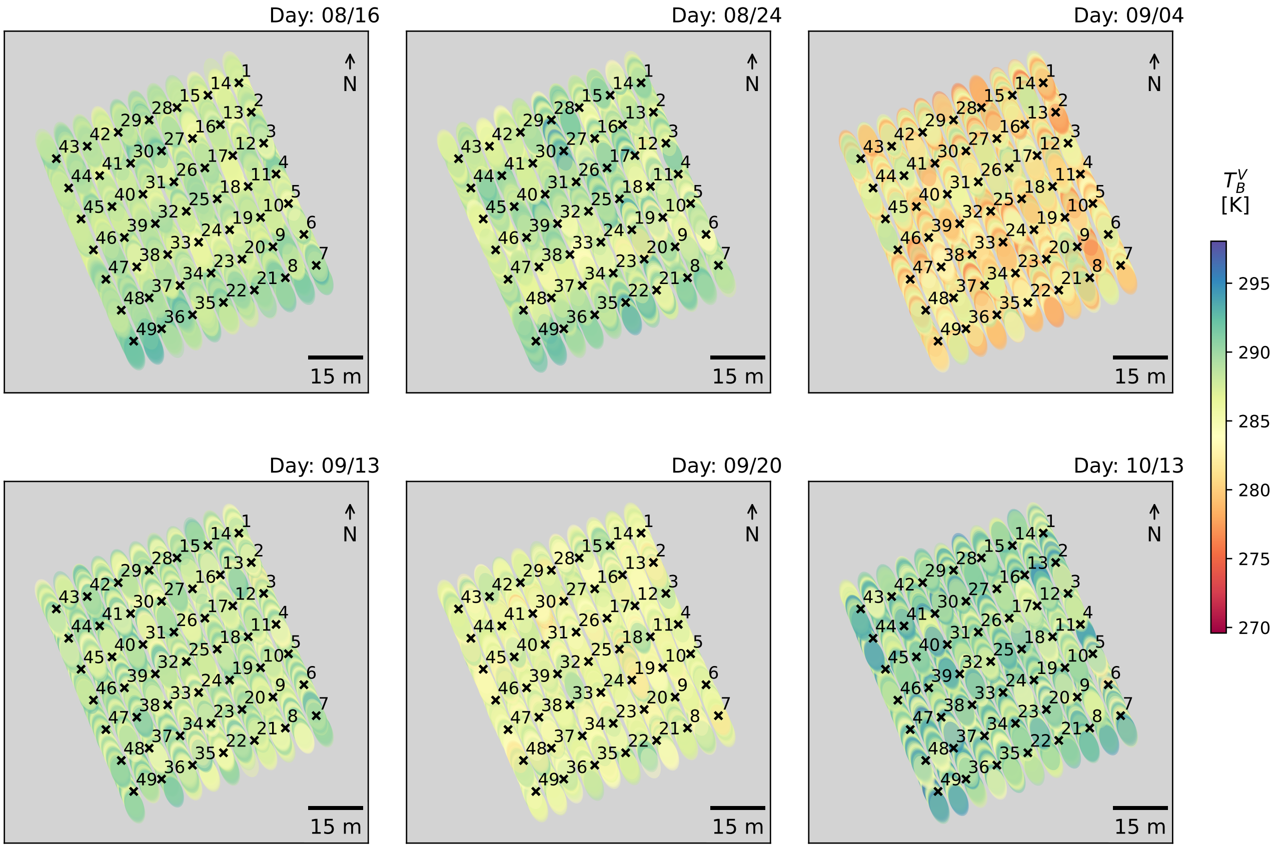

Figure 4.7: Map of L-band vertical polarization brightness temperature observations. Each point represents the center of the projected radiometer footprint with a 4.5 m diameter.

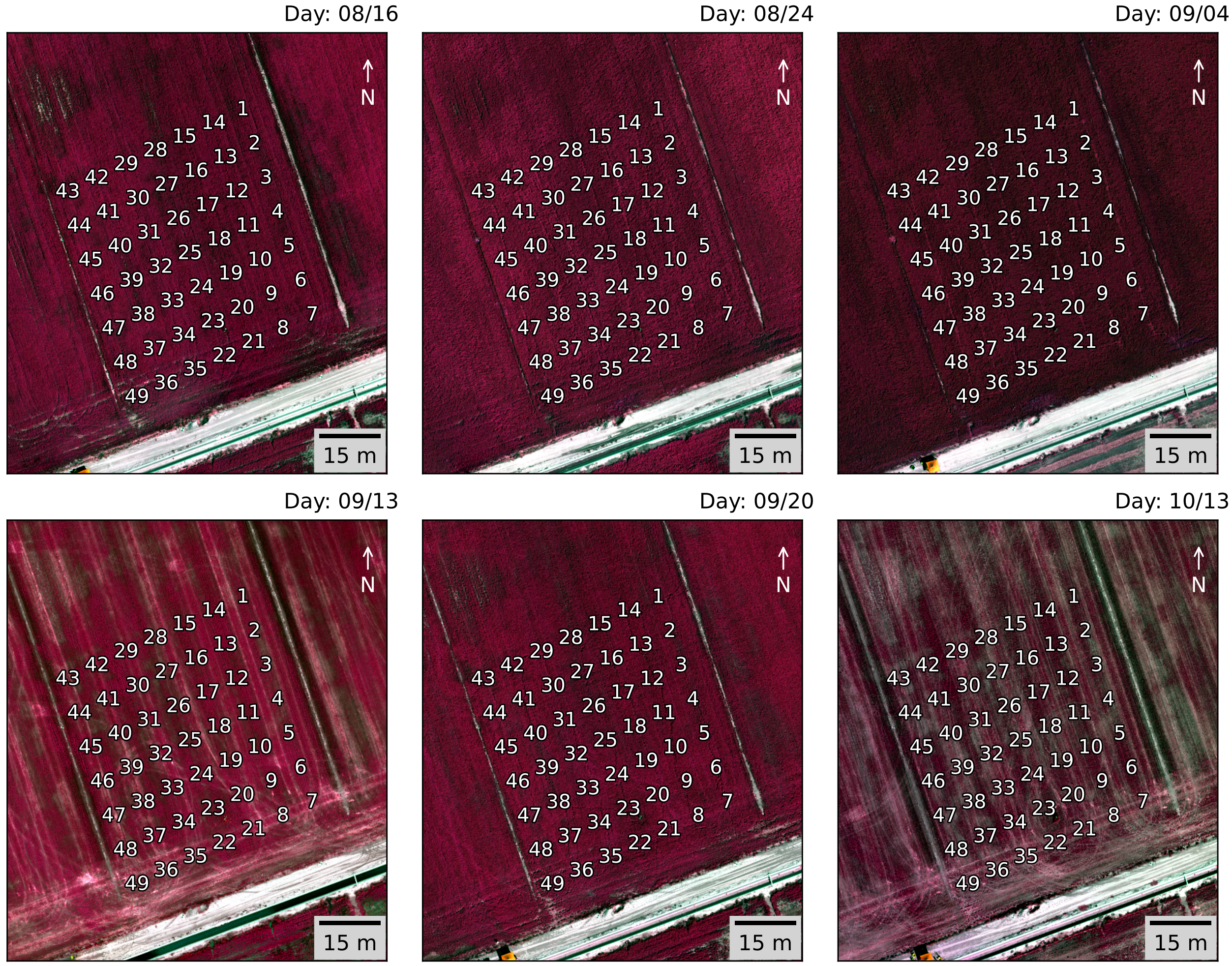

Figure 4.8: False color infrared orthophotos over the study area for the campaigns conducted from August to October 2023 at the Chamberino, New Mexico's alfalfa crops. Maps near IR, red, and green are red, green, and blue (RGB).

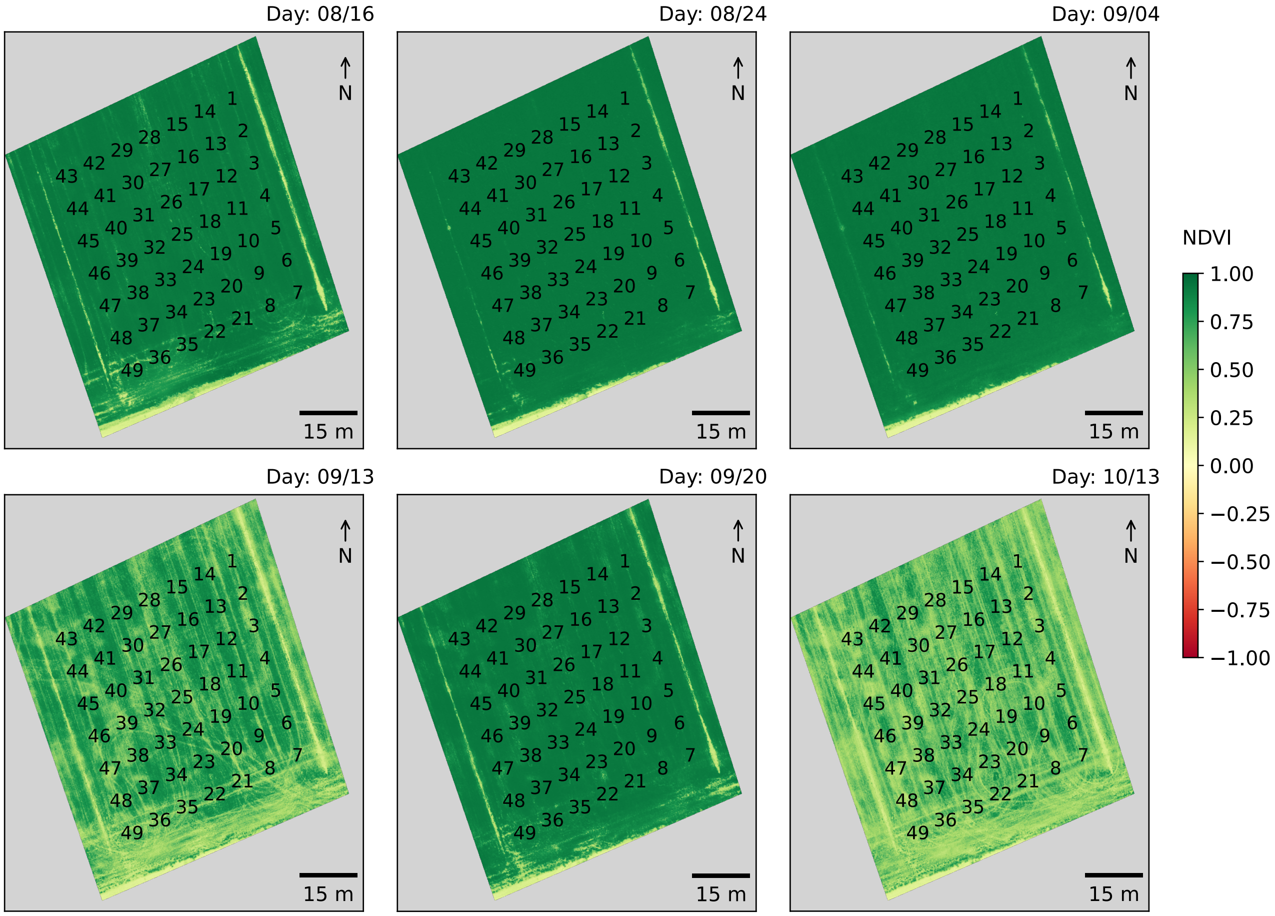

Day: 08/16

Day: 08/24

Day: 09/04

Day: 09/13

Day: 09/20

Day: 10/13

Figure 4.9: Map of NDVI observations over the study site (alfalfa) during the field campaigns conducted from August to October 2023 at Chamberino, New Mexico.

4.2 Model Training

The single channel and dual channel algorithms were tuned using the volumetric soil moisture data from section 4.5 and τ derived from multi-spectral imagery (NDVI-τ) shown in Figure 4.9, finding through 2,583 different iterations of roughness parameters HQN, the combinations that minimized the loss function (Equation 3.7) for every brightness temperature measurement. Two groups of models with the best RMSE for soil moisture were selected. A first group, where the roughness parameters were iterated freely (see Figure 4.10), and a second batch of models (see Figure 4.11) where the roughness intensity effects (H) were more significant than the polarization mixing effects (Q), common assumption in similar modeling efforts (Dai et al., 2021; Ye et al., 2024). The testing scores for the models are presented in Table 4.2. Unrestricted calibrations outperformed restricted models for dual and horizontal polarization retrieval and equaled the metrics for vertical antenna retrievals. Additional metrics such as the unbiased root mean square error (ubRMSE), the bias, the mean absolute error (MAE), the Kling-Gupta Efficiency (KGE), the correlation coefficient (R), and the coefficient of determination (R^2), were included to provide additional understanding of the model behavior and limitations. Using additional metrics such as the ubRMSE provides insights into the model's ability to replicate soil moisture's time variability even under biased mean estimations or dynamic ranges (Entekhabi, Reichle, et al., 2010).

Table 4.2: Testing metrics for all the calibrated soil moisture retrieval models. Best statistic of each row in bold.

			H>Q			no restriction		
Metrics	Units	Best score	Dual-pol	H-pol	V-pol	Dual-pol	H-pol	V-pol
Bias	cm^3/cm^3	0	-0.049	-0.076	**0.001**	-0.023	-0.043	**0.001**
MAE	cm^3/cm^3	0	0.055	0.078	0.052	**0.043**	0.049	0.052
RMSE	cm^3/cm^3	0	0.066	0.087	0.065	**0.054**	0.059	0.065
ubRMSE	cm^3/cm^3	0	0.044	0.042	0.065	0.049	**0.039**	0.065
R2	-	1	0.715	0.503	0.717	**0.807**	0.773	0.717
R	-	1	0.934	**0.947**	0.850	0.926	**0.947**	0.850
KGE	-	1	0.800	0.699	0.731	0.775	**0.825**	0.731

While the V-polarization retrieval model performed identically with the restriction, the Dual-polarization and the single H-polarization performances decreased (relative to

RMSE). Vertical models were the least biased and had greater errors due to more dispersed retrievals. Dual and H polarization models underestimated moisture for all the campaign dates except by Oct. 10^{th}. All non-restricted models performed better for dry days (below 0.2 cm^3/cm^3) as depicted in Figures 4.12 and 4.13 . Table 4.3 summarizes the best HQN parameters for the best-performing models.

Table 4.3: Calibrated roughness parameters for best-fit soil moisture retrievals separated by two groups, a set of models with H >Q and a set of unrestricted roughness parameters.

	H >Q			no restriction		
Roughness parameters	Dual-pol	H-pol	V-pol	Dual-pol	H-pol	V-pol
H	0.40	0.30	0.50	0.05	0.00	0.50
Q	0.35	0.25	0.00	1.00	0.75	0.00
N	2.00	2.00	1.00	0.00	0.00	1.00

Generally, lower values of roughness intensity converged with higher values of polarization mixing effects. H maintained between 0.3 and 0.5 for restrained models, but its non-restricted counterparts had lower roughness intensity values, behaving like smooth surfaces with a higher mixing effect. The angular effects in reflectivity did not significantly affect the models' performance, and all $N = 0, 1, 2$ values were present at least in one of the best-performing models. Restricted models had higher roughness angular effects.

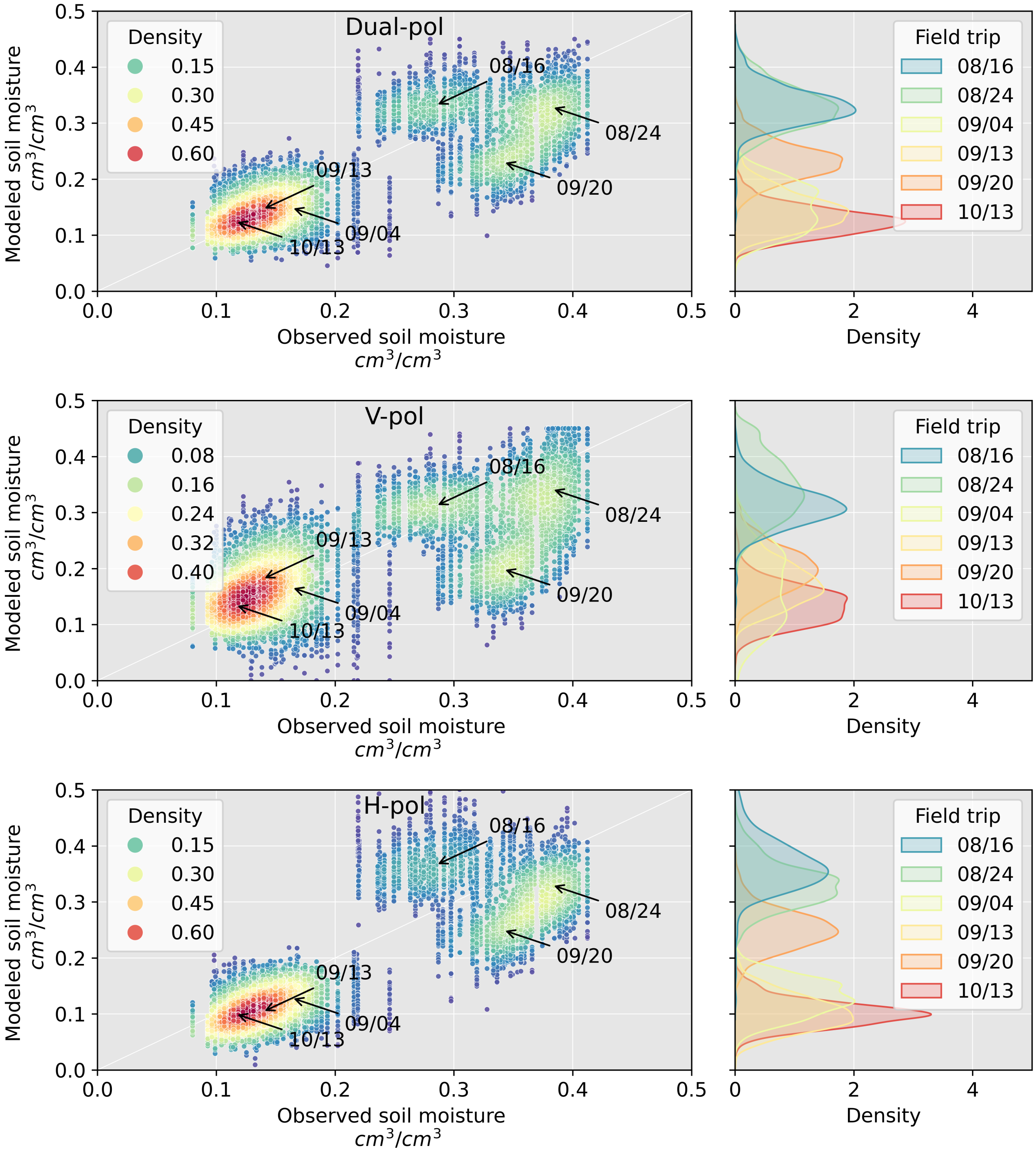

Figure 4.10: Observed vs. modeled 12cm soil moisture retrievals with the non-restricted calibrated radiative transfer models, color-coded by density. Vertical kernel density functions of modeled soil moisture by day.

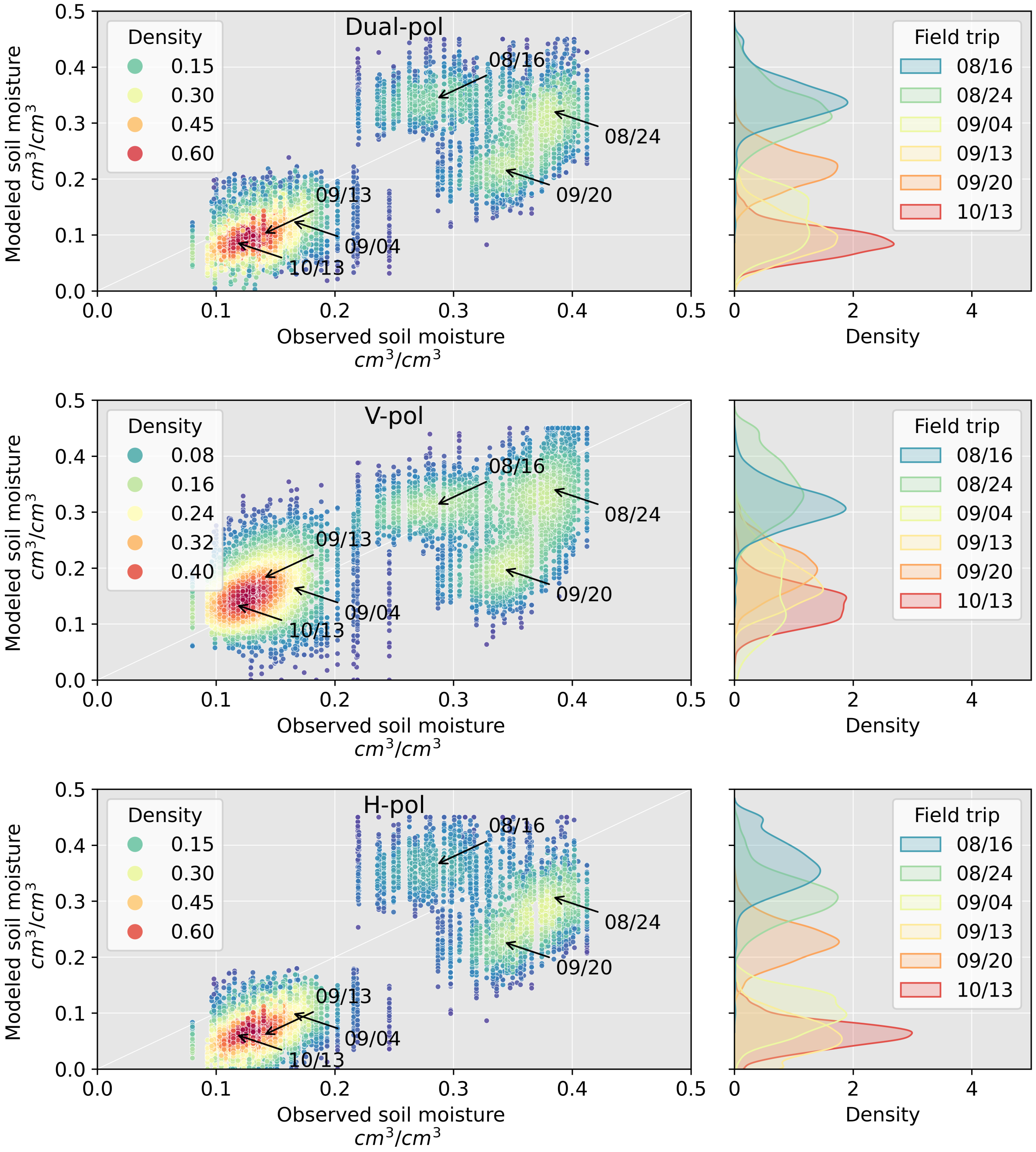

Figure 4.11: Observed vs. modeled 12 cm soil moisture retrievals with (H>Q) calibrated radiative transfer models, color-coded by density. Vertical kernel density functions of modeled soil moisture by day.

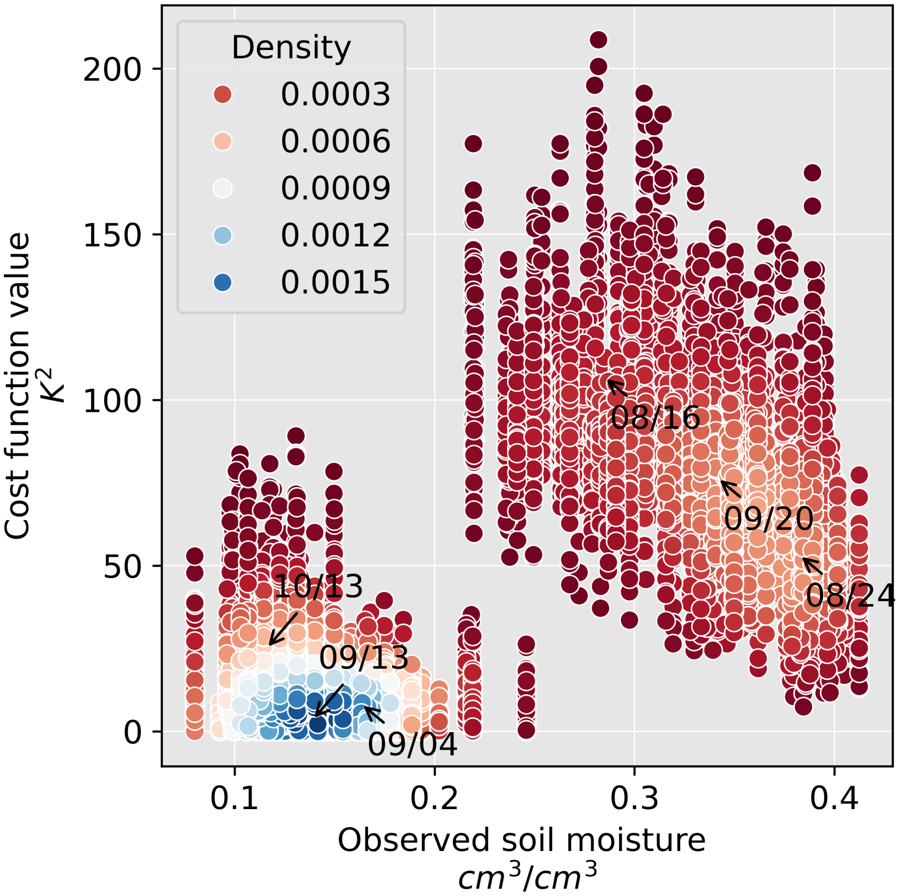

Figure 4.12: Observed 12 cm soil moisture vs Cost function value (equation 3.7) for the best RMSE dual polarization model retrievals.

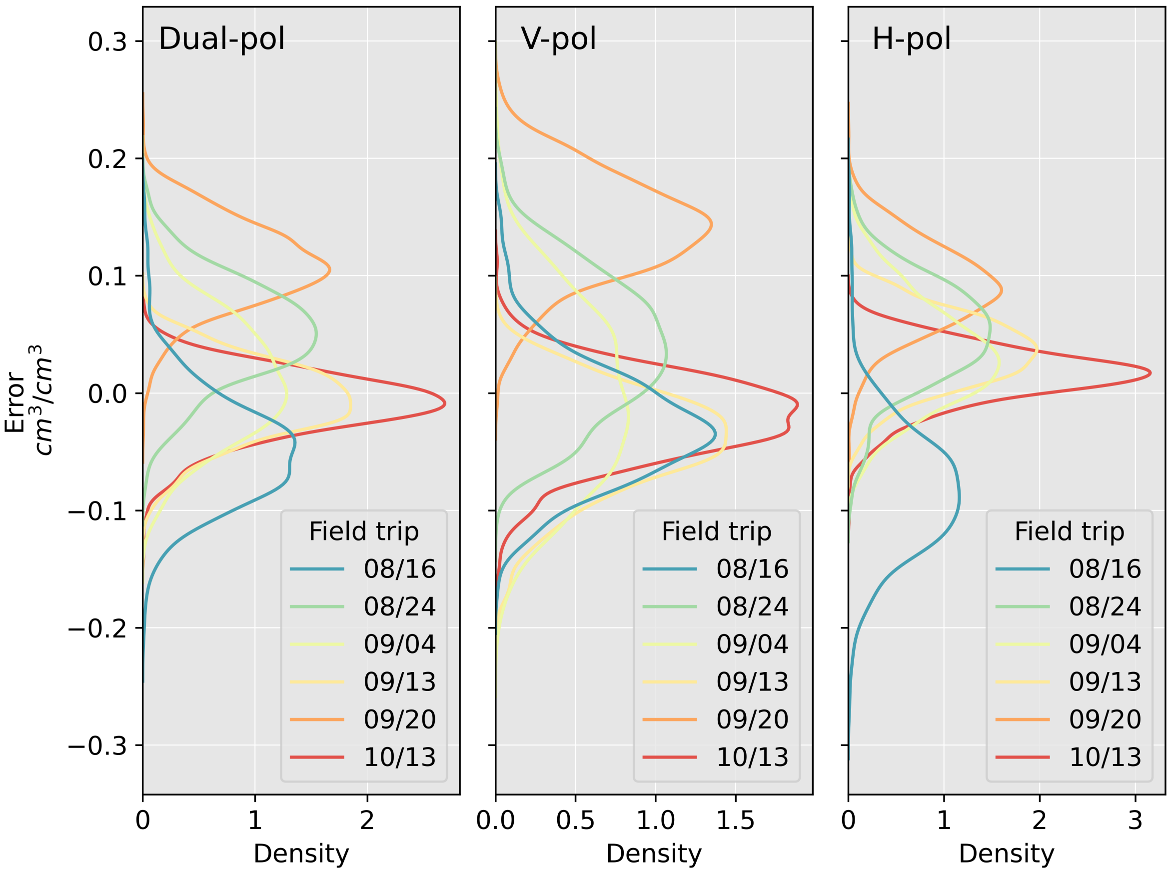

Figure 4.13: Vertical kernel density functions of 12 cm soil moisture error distribution grouped by field days. Errors for the best performing Dual (Dual-pol), and single horizontal (H-pol) and vertical (V-pol) trained models.

4.3 Model Testing

Figure 4.14 presents the spatial distribution of the retrievals for all unrestricted trained performing models. Generally, horizontal polarization models presented dryer retrievals on the dryer days and wetter retrievals on the higher moisture days, compared to V and Dual models. Horizontal retrievals presented more spatially homogeneous data, while vertical and dual retrievals had more local spatial variations.

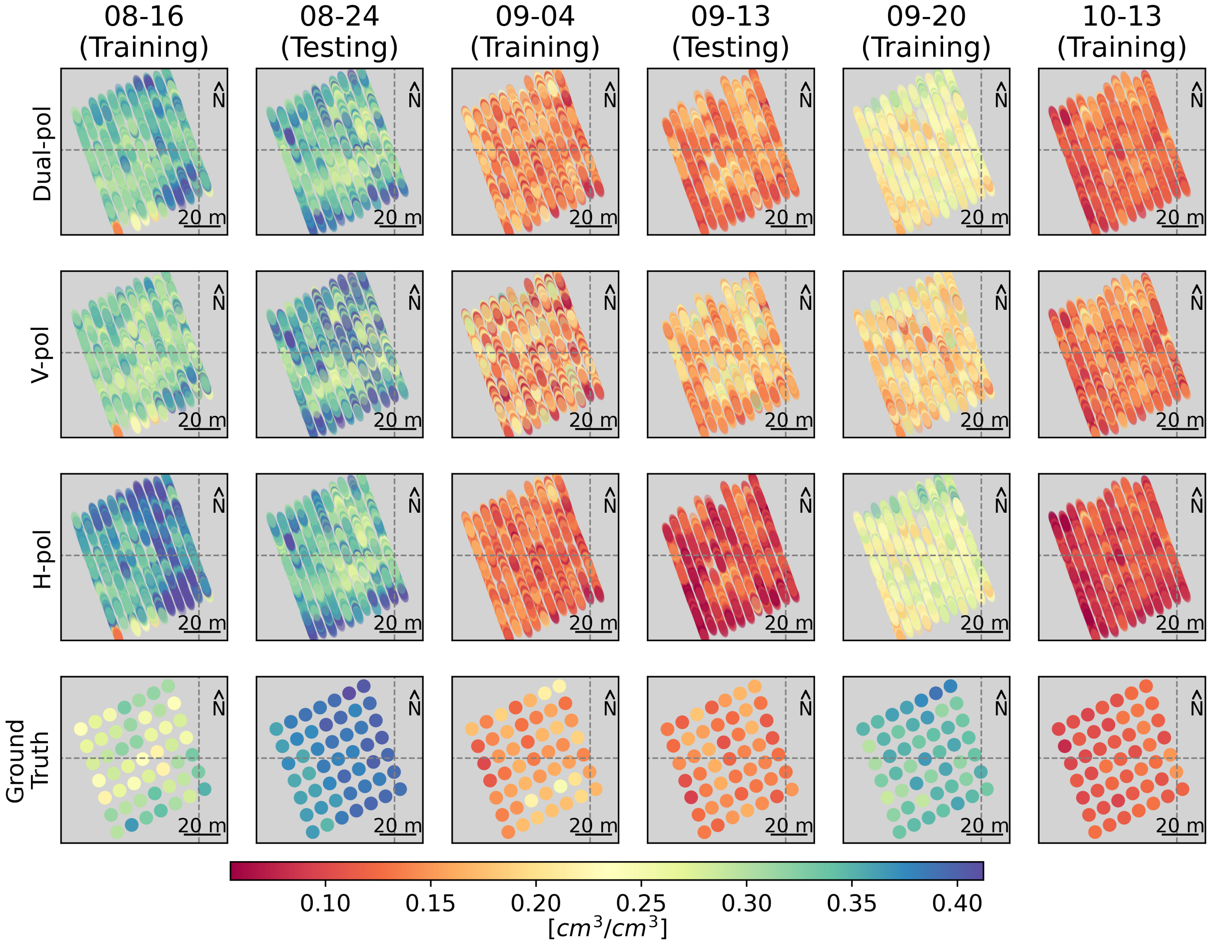

Figure 4.14: Map of three retrieved 12 cm soil moisture for the best performing Dual (Dual-pol), single horizontal (H-pol) and vertical (V-pol) trained models, and measured 12cm soil moisture.

Table 4.4 presents the assessment metrics for each day, split, and overall. Specifically, the days Sept. 4^{th}, Sept. 13^{th}, and Oct. 13^{th} presented better bias, mean absolute error (MAE), root mean square error (RMSE), and unbiased RMSE (ubRMSE) compared to Aug. 16^{th}, Aug. 24^{th}, and Sept. 20^{th}. Overall, the combined evaluation of multiple days, such as in training, testing, or considering all days together, consistently outperformed individual day evaluations. This trend suggests that the model excels in predicting variations over time rather than capturing spatial differences within the same day.

The model performed well in testing, with a slight underestimation indicated by a bias of -0.023 cm^3/cm^3. Accuracy metrics, including mean absolute error (MAE) and root mean square error (RMSE), were low at 0.043 cm^3/cm^3 and 0.054 cm^3/cm^3, respectively, highlighting accurate predictions. The unbiased RMSE (ubRMSE) was 0.049 cm^3/cm^3, signifying consistent performance. A strong correlation between predicted and observed values was evidenced by a R^2 value of 0.807, while the correlation coefficient (R) was high at 0.926. The Kling-Gupta Efficiency (KGE) index was 0.775, indicating robust overall performance. The model demonstrated a reliable and accurate representation of underlying data patterns during testing. Although the horizontal polarization model performed best in the testing split for ubRMSE, R, and KGE, the H-pol model performance dropped below the Dual-pol when the entirety of the data was evaluated. The dual polarization model with HQN = 0.05, 1.00, 0.00 presented the minimum ubRMSE of the study when evaluating the data for all the campaigns.

Table 4.4: Evaluation metrics by day for soil moisture retrievals with the best performing dual polarization model with HQN = 0.05, 1.00, 0.00. Aug. 16^{th}, Sept. 4^{th}, Sept. 20^{th} and Oct. 10^{th} were used for training. Aug. 24^{th} and Sept. 13^{th} were used for testing, for a 66.66%, 33.33% split.

Fieldtrip	Bias	MAE	RMSE	ubRMSE	R^2	R	KGE
08-16	0.047	0.058	0.069	0.050	-2.932	0.008	-0.007
08-24	-0.052	0.058	0.068	0.043	-19.432	-0.114	-0.954
09-04	-0.013	0.043	0.054	0.052	-2.082	-0.033	-0.093
09-13	**0.007**	0.027	0.034	0.033	-2.409	0.278	-0.085
09-20	-0.109	0.109	0.115	0.036	-25.438	0.205	**0.018**
10-13	0.010	**0.023**	**0.030**	**0.028**	-3.352	0.112	-0.202
All	**-0.017**	**0.051**	**0.066**	**0.064**	**0.615**	**0.803**	**0.757**
Testing	-0.023	0.043	0.054	0.049	0.807	0.926	0.775
Training	-0.013	0.056	0.071	0.070	0.420	0.704	0.692
Units	cm^3/cm^3	cm^3/cm^3	cm^3/cm^3	cm^3/cm^3	-	-	-

4.4 Model Parameter Sensitivity Analysis

To determine the sensitivity of both polarization brightness temperatures, the historical six years (2016-2022) of SMAP products (see Figure 3.1) were analyzed to set iteration boundaries for a one-at-a-time OAT sensitivity analysis displayed on a sensitivity tornado (see Figure 4.15). Based on the results, soil moisture was the variable that contributes the most to changes in brightness temperature values, supporting the model's suitability for retrieving soil moisture from L-band T_B. The impact of the incidence angle on measurements had a crucial consideration, as it significantly affected the accuracy of the modeled data. However, for UAS operations, this variable represented a challenging and uncontrolled condition due to the system's large size that made using a generic gimbal infeasible.

Moreover, real-time correction of inclinations resulting from wind gusts was not possible, further complicating the management of this factor.

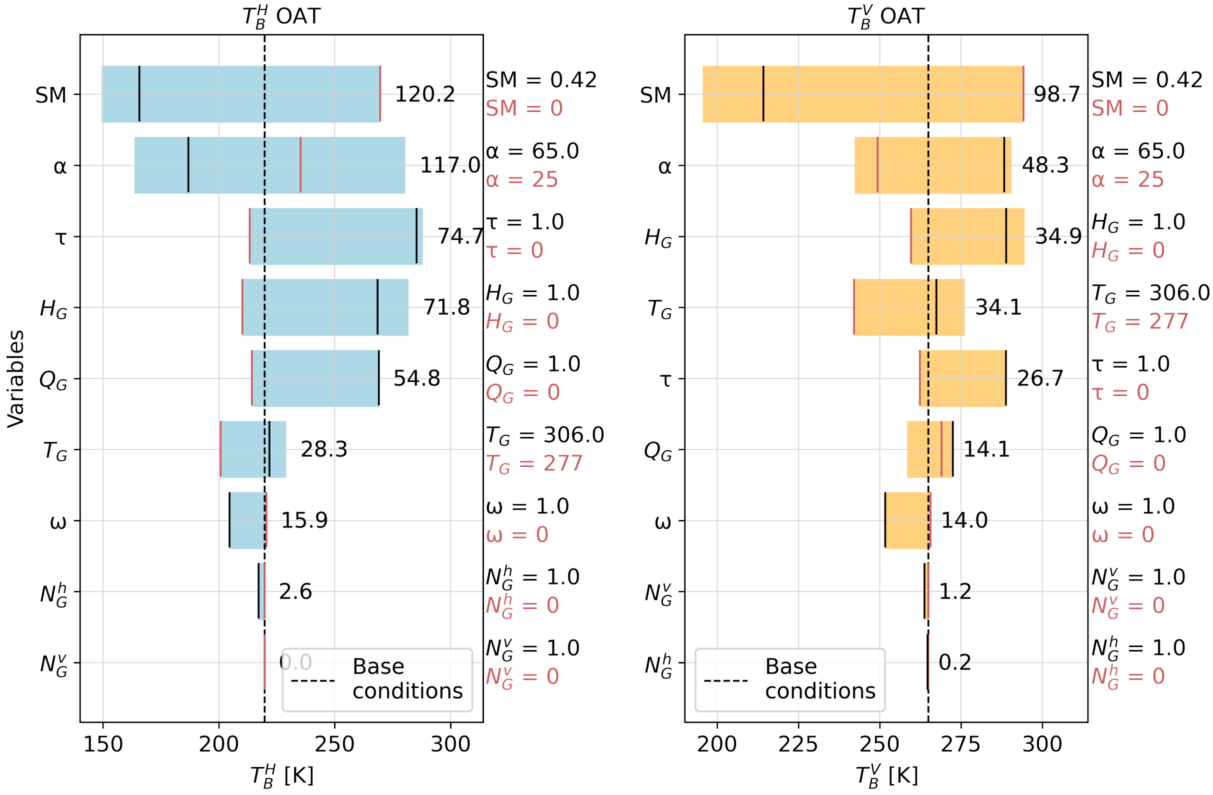

Figure 4.15: One at a time T_B sensitivity to model parameters (in red: minimum values from SMAP/SMOS, in black: maximum values from SMAP/SMOS). With base conditions: soil moisture (SM) = 0.17, vegetation opacity (τ) = 0.03, nadir angle (α) = 44°, soil temperature (ST) = 303.15, Roughness parameters (HQN), hG = 0.11, qG = 0.1, nGv = 0, nGh = 0.

The impact of vegetation opacity on the accuracy of polarization readings was a crucial factor to consider. Horizontal polarization readings were more susceptible to this effect than their vertical counterparts. Conversely, the sensitivity of vertical polarization readings to variations in the roughness semi-empirical parameter H was greater than that of horizontal polarization. Therefore, proper consideration and interpretation of these distinct effects is recommended for accurate measurements in scenarios where vegetation and roughness conditions play a significant role.

4.5 Effects of roughness

Calibrating the roughness parameter is deemed crucial for obtaining reliable soil moisture retrievals. Utilizing the Portable L-band Radiometer (PoLRa) without calibration based on lookup parameters from the Soil Moisture Active Passive (SMAP) algorithm can lead to retrievals with high errors. Figures 4.16 and 4.17 depict changes in model testing performance for various combinations of roughness intensity (H), polarization mixing effect (Q), and angular dependency (N) values. A comparison with the bias is also included in figure A.1.

For the dual and horizontal polarization model, there was an observed trend of performance improvement with the decrease of H and the increase of Q. The relationship between the coefficient of determination (R^2). H exhibited a bell-shaped curve that became steeper with the decrease of N values and attained its maximum with the increase of Q relative to H. Conversely, the R^2 for vertical polarization models exhibited two peaks, one for $H > Q$ and another for $Q > H$. This behavior, as described by the relations in Equation 3.4, demonstrates the dominant contribution of the vertical component of the Fresnel reflectivity for achieving better-performing retrievals.

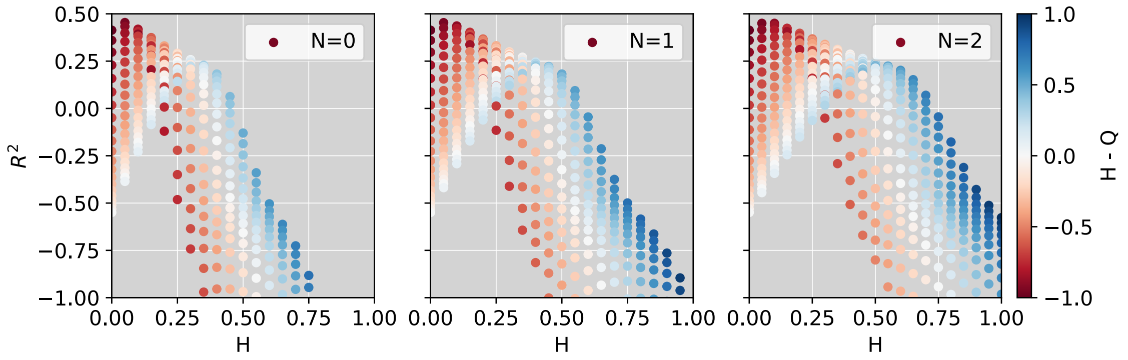

(a) Dual polarization.

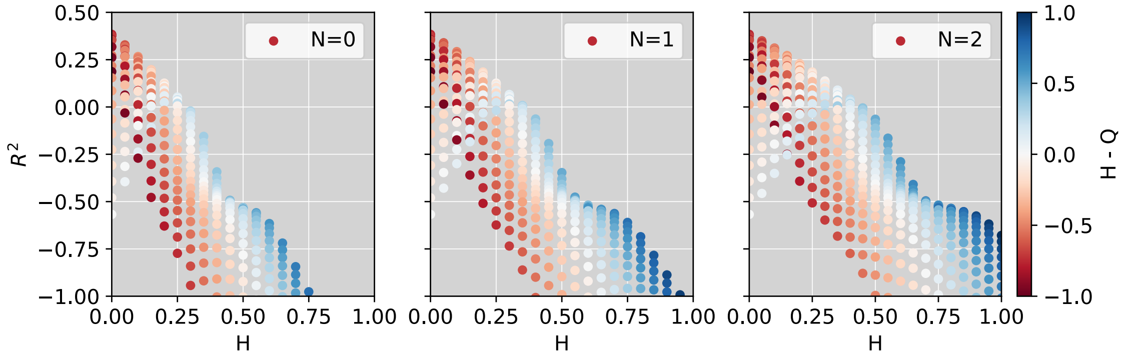

(b) Horizontal polarization.

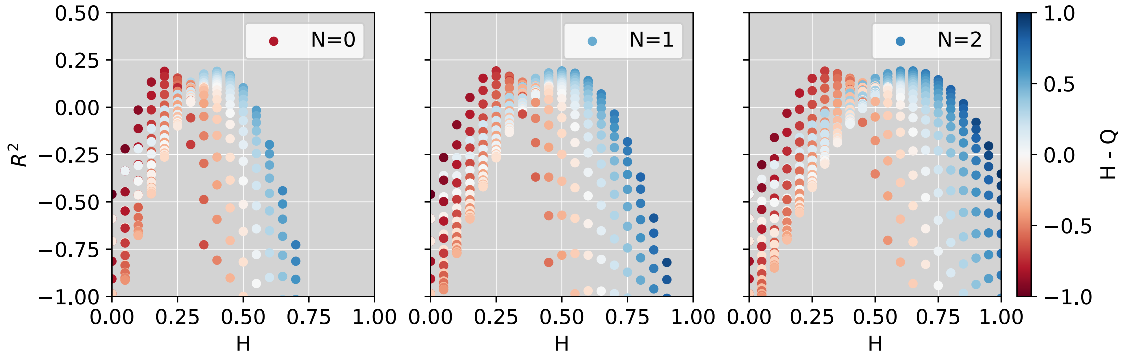

(c) Vertical polarization.

Figure 4.16: H vs R^2 during the training phase for (a) dual polarization, (b) single horizontal and (c) vertical soil moisture retrievals with N = 0,1,2, colored by H−Q to distinguish trends for different relations between H and Q.

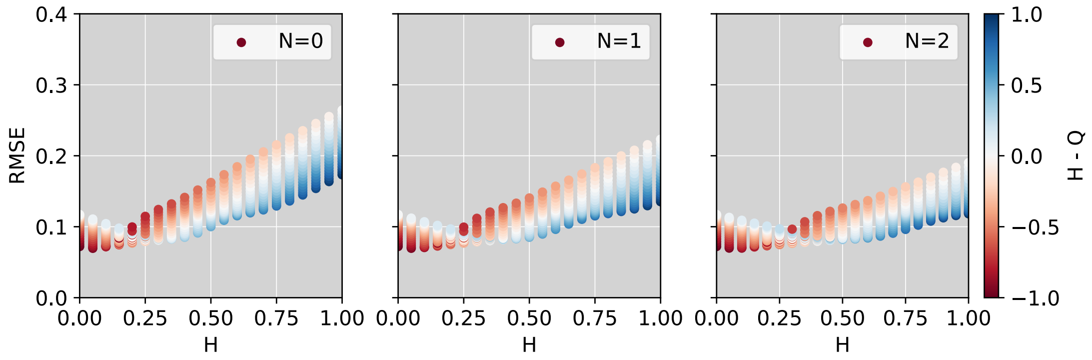

(a) Dual polarization.

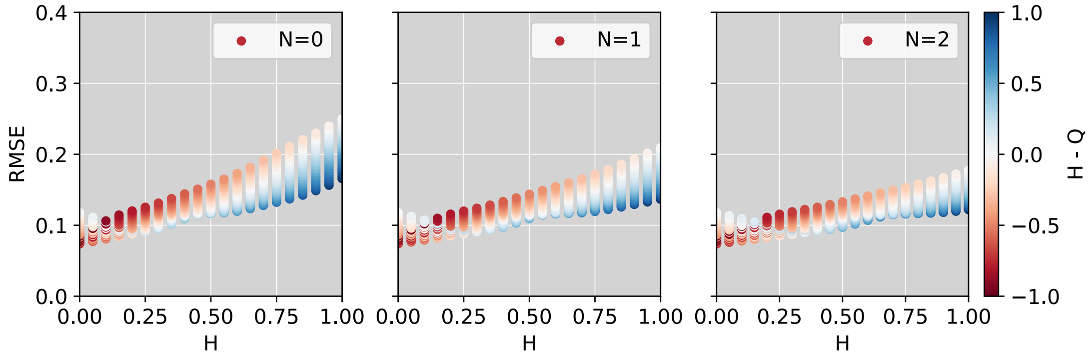

(b) Horizontal polarization.

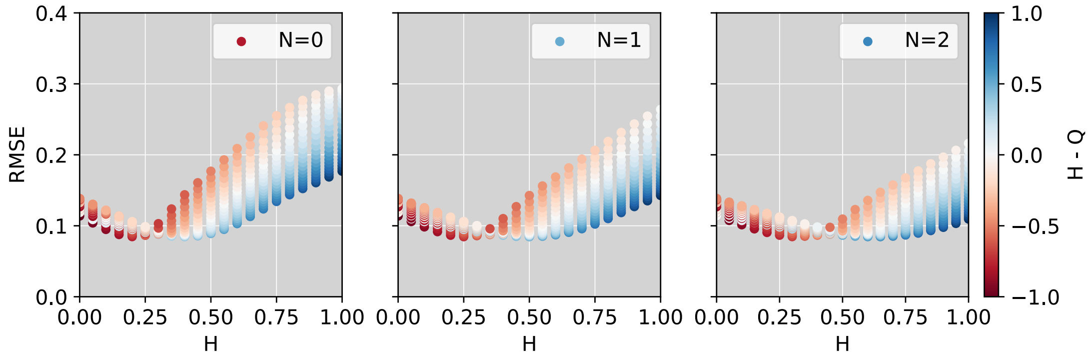

(c) Vertical polarization.

Figure 4.17: H vs RMSE during the training phase for (a) dual polarization, (b) single horizontal and (c) vertical soil moisture retrievals with N = 0,1,2, colored by H−Q to distinguish trends for different relations between H and Q.

Chapter 5

Discussion

This study presented a high-resolution ground truth validated tau-omega microwave emission modeling effort for soil moisture retrievals with a UAS-mounted L-band radiometer and multi-spectral camera over alfalfa fields. It is a novel approach that used low-altitude (7 m AGL) hexacopter microwave readings with a non-interpolated radiometer's footprint resolution of 4.5 m, validated with a 7 m separation grid 12cm surface soil moisture and utilizes the Portable L-band Radiometer (PoLRa). Due to the limited availability of similar approaches, comparison with prior studies reveals differences in various factors, including the type of platform used (satellite, aircraft, or fixed-wing UAS), the radiometer employed, the complementary data integrated (multi-spectral, thermal, hyper-spectral), spatial and temporal resolution, altitude, land cover, the number of flights, and the model and algorithm architecture utilized. For instance, Ye et al. (2024) used a low-elevation (225 m) aircraft to simulate UAV missions, validated with top 5 cm, and obtained a RMSE of 0.05-0.06 cm^3/cm^3 for 38.5° nadir L-band at a 75 m grid. This study also retrieved moisture from thermal-optical with an RMSE of 0.05-0.09 cm^3/cm^3. Similarly, Sanchez et al. (2014) used a low-elevation small aircraft with a novelty approach that linearly mixed surface temperature, vegetation indexes from hyper-spectral imagery, and L-band brightness temperature. At a 3.5 m spatial resolution, correlations above 0.76 and an RMSE below 0.07 cm^3/cm^3 were achieved. Furthermore, Dai et al. (2021) presented a comprehensive similar approach with a fixed-wing radiometer, achieving a correlation coefficient of 0.69 with 10 cm soil moisture. The theoretically estimated errors of the experiment were between 5.41% and 7.33% for different land covers. Pioneering the UAS microwave surveying, Acevo-Herrera et al. (2010) used a fixed-wing L-band (100 m footprint) radiometer to estimate 5 cm soil moisture with absolute errors between 1-6% and 1-9% for two different sites. Generally, an ubRMSE $\leq 0.04\,\mathrm{m}^3/\mathrm{m}^3$ and a R ≥ 0.7 is expected for both the SMAP and SMOS satellite missions (Chen et al., 2019; Panciera et al., 2009). With grid sizes of 33 km and 35-50 km, and incidence angles of 40° and 0-55° (Chan et al., 2012; Kerr et al., 2012). This performance is guaranteed for vegetation water content $\geq$ 5 kg/m^2(for SMAP) and can vary depending on local variables, flags, and calibration schemes.

5.1 Retrieval Accuracy

During the testing phase, this study achieved a RMSE 0.054 cm^3/cm^3, a ubRMSE of 0.049 m^3/m^3, and a correlation of 0.807. The model better predicted the average soil moisture for dry days (Sept. 4th, Sept. 13th, Oct. 13th). However, it overestimated the moisture on Aug. 16th and underestimated it on Sept. 20th and Aug. 24th (wet days). Despite having a significant amount of outliers each day, the overall trend of the retrievals in Figure 4.10 expresses the ability of the model to capture the mean surface soil moisture under various moisture and vegetation conditions. As expected, the models' retrievals inherit the noise present in remotely sensed data. Figure 5.1 shows the spatial distribution of the best-performing model in the study where the noise inherited from brightness temperature data is noticeable in all the readings. Additionally, the water intercepted by the vegetation during the precipitation events of Aug. 24th and Aug. 16th could potentially generate noise as indicated by Kerr et al. (2012). Furthermore, the probe validation data could present an unaccounted noise in conditions of high vertical variability, thus accentuating the difference for days with high surface soil moisture in which the existence of shallow water can affect the penetration of the remote sensing retrievals.

Figure 5.2 illustrates the correlation between the study variables' daily mean and standard deviation and the model's retrieval performance metrics for each day. A notable negative correlation of -0.81 exists between the mean measured soil moisture and the model's R^2, indicating that the model estimates moisture on drier days with ease compared to high moisture days. Additionally, a positive correlation of 0.80 between the mean daily HSII readings and the root mean square error (RMSE) and a positive correlation of 0.72 between the HSII mean daily readings and the mean daily NDVI. The variables with the highest (absolute value) correlation to the mean daily HSII readings were last irrigation day (-0.94), mean NDVI (0.75), and horizontal L-band brightness temperature (-0.64). Implementing data-driven machine learning algorithms to estimate soil moisture using highly correlated variables could potentially present a feasible alternative approach to the semi-empirical effort developed in this study, bypassing the complexity of the microwave emission models.

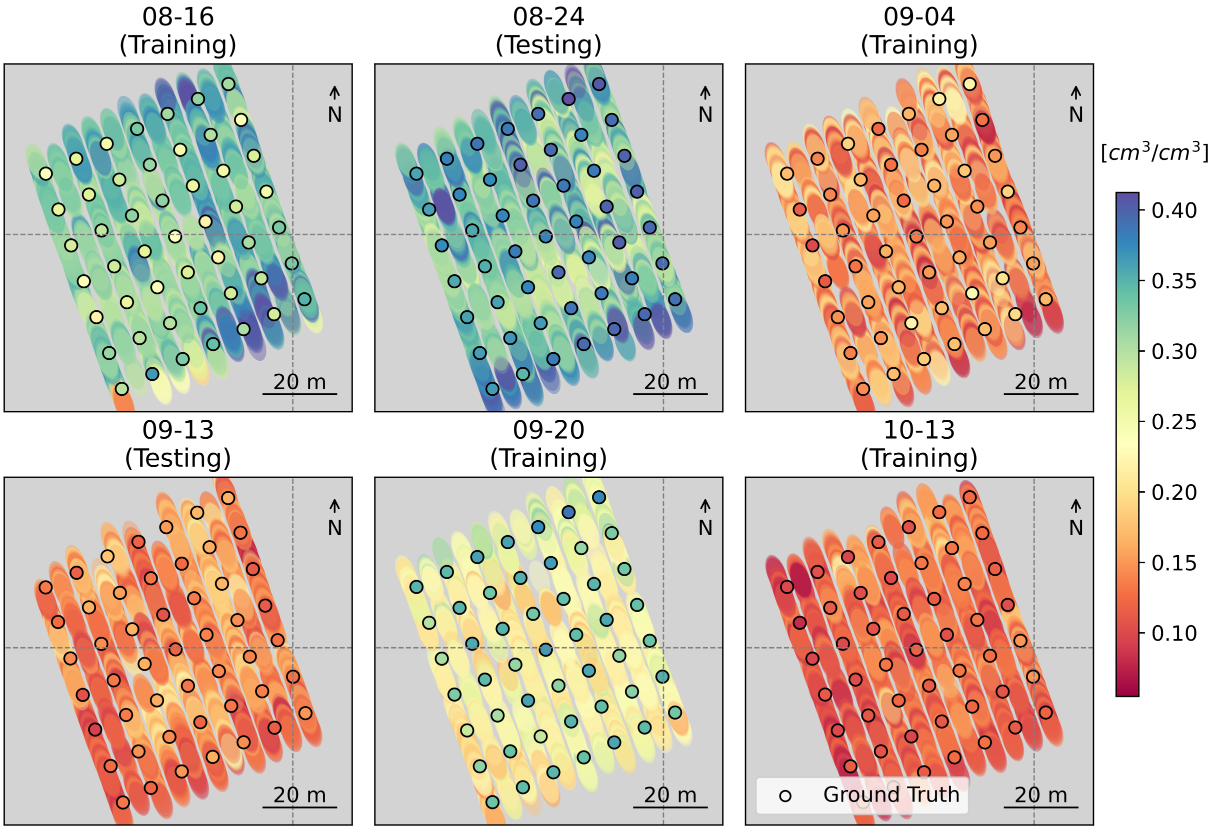

Figure 5.1: Map of measured ground truth moisture over best-performing model retrieval: Dual-polarization, with HQN = {0.05, 1.00, 0.00}.

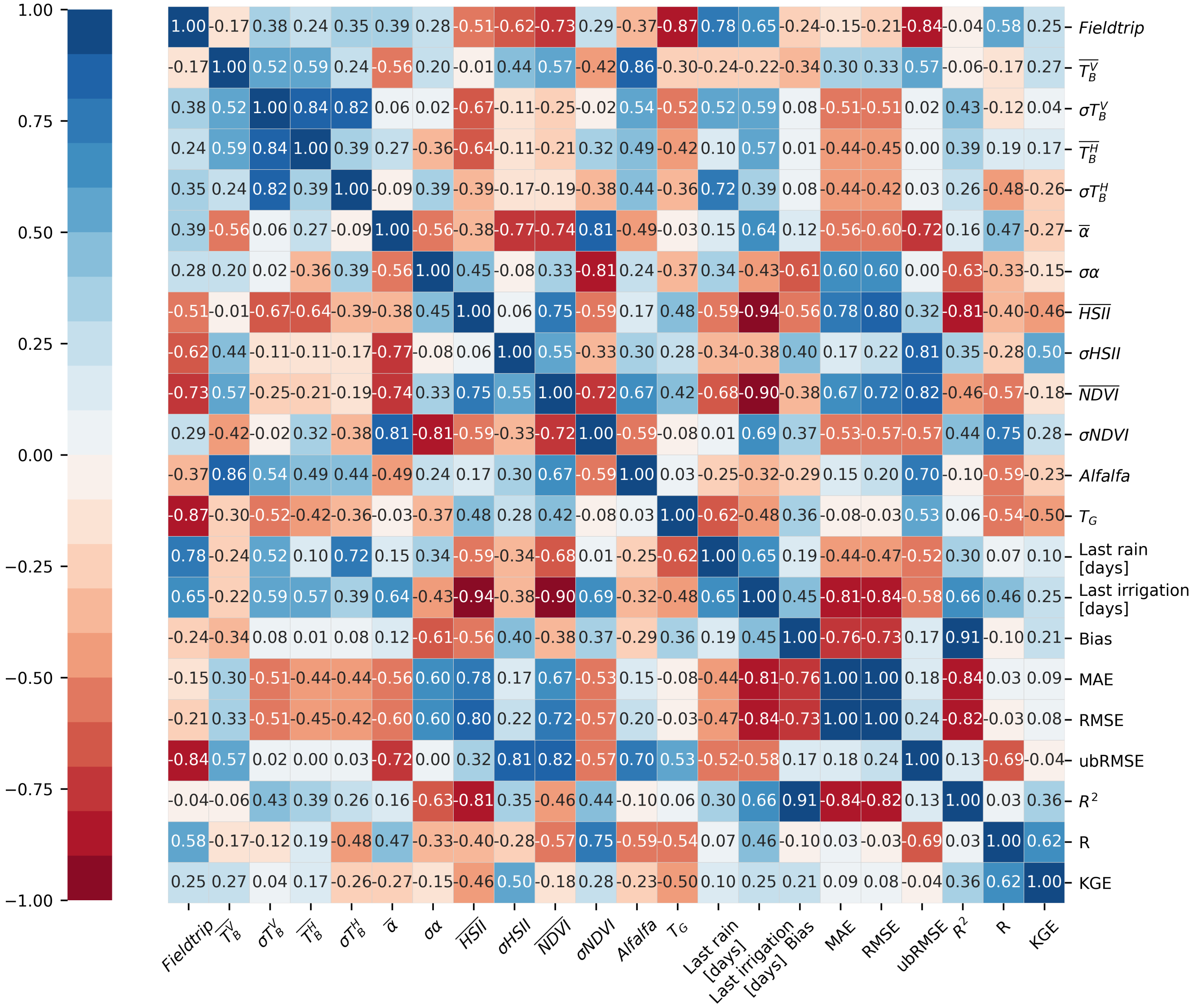

	Fieldtrip	$\overline{T_B^V}$	σT_B^V	$\overline{T_B^H}$	σT_B^H	$\overline{\alpha}$	$\sigma\alpha$	$\overline{HSII}$	$\sigma HSII$	$\overline{NDVI}$	$\sigma NDVI$	Alfalfa	T_G	Last rain [days]	Last irrigation [days]	Bias	MAE	RMSE	ubRMSE	R^2	R	KGE
Fieldtrip	1.00	-0.17	0.38	0.24	0.35	0.39	0.28	-0.51	-0.62	-0.73	0.29	-0.37	-0.87	0.78	0.65	-0.24	-0.15	-0.21	-0.84	-0.04	0.58	0.25
$\overline{T_B^V}$	-0.17	1.00	0.52	0.59	0.24	-0.56	0.20	-0.01	0.44	0.57	-0.42	0.86	-0.30	-0.24	-0.22	-0.34	0.30	0.33	0.57	-0.06	-0.17	0.27
σT_B^V	0.38	0.52	1.00	0.84	0.82	0.06	0.02	-0.67	-0.11	-0.25	-0.02	0.54	-0.52	0.52	0.59	0.08	-0.51	-0.51	0.02	0.43	-0.12	0.04
$\overline{T_B^H}$	0.24	0.59	0.84	1.00	0.39	0.27	-0.36	-0.64	-0.11	-0.21	0.32	0.49	-0.42	0.10	0.57	0.01	-0.44	-0.45	0.00	0.39	0.19	0.17
σT_B^H	0.35	0.24	0.82	0.39	1.00	-0.09	0.39	-0.39	-0.17	-0.19	-0.38	0.44	-0.36	0.72	0.39	0.08	-0.44	-0.42	0.03	0.26	-0.48	-0.26
$\overline{\alpha}$	0.39	-0.56	0.06	0.27	-0.09	1.00	-0.56	-0.38	-0.77	-0.74	0.81	-0.49	-0.03	0.15	0.64	0.12	-0.56	-0.60	-0.72	0.16	0.47	-0.27
$\sigma\alpha$	0.28	0.20	0.02	-0.36	0.39	-0.56	1.00	0.45	-0.08	0.33	-0.81	0.24	-0.37	0.34	-0.43	-0.61	0.60	0.60	0.00	-0.63	-0.33	-0.15
$\overline{HSII}$	-0.51	-0.01	-0.67	-0.64	-0.39	-0.38	0.45	1.00	0.06	0.75	-0.59	0.17	0.48	-0.59	-0.94	-0.56	0.78	0.80	0.32	-0.81	-0.40	-0.46
$\sigma HSII$	-0.62	0.44	-0.11	-0.11	-0.17	-0.77	-0.08	0.06	1.00	0.55	-0.33	0.30	0.28	-0.34	-0.38	0.40	0.17	0.22	0.81	0.35	-0.28	0.50
$\overline{NDVI}$	-0.73	0.57	-0.25	-0.21	-0.19	-0.74	0.33	0.75	0.55	1.00	-0.72	0.67	0.42	-0.68	-0.90	-0.38	0.67	0.72	0.82	-0.46	-0.57	-0.18
$\sigma NDVI$	0.29	-0.42	-0.02	0.32	-0.38	0.81	-0.81	-0.59	-0.33	-0.72	1.00	-0.59	-0.08	0.01	0.69	0.37	-0.53	-0.57	-0.57	0.44	0.75	0.28
Alfalfa	-0.37	0.86	0.54	0.49	0.44	-0.49	0.24	0.17	0.30	0.67	-0.59	1.00	0.03	-0.25	-0.32	-0.29	0.15	0.20	0.70	-0.10	-0.59	-0.23
T_G	-0.87	-0.30	-0.52	-0.42	-0.36	-0.03	-0.37	0.48	0.28	0.42	-0.08	0.03	1.00	-0.62	-0.48	0.36	-0.08	-0.03	0.53	0.06	-0.54	-0.50
Last rain [days]	0.78	-0.24	0.52	0.10	0.72	0.15	0.34	-0.59	-0.34	-0.68	0.01	-0.25	-0.62	1.00	0.65	0.19	-0.44	-0.47	-0.52	0.30	0.07	0.10
Last irrigation [days]	0.65	-0.22	0.59	0.57	0.39	0.64	-0.43	-0.94	-0.38	-0.90	0.69	-0.32	-0.48	0.65	1.00	0.45	-0.81	-0.84	-0.58	0.66	0.46	0.25
Bias	-0.24	-0.34	0.08	0.01	0.08	0.12	-0.61	-0.56	0.40	-0.38	0.37	-0.29	0.36	0.19	0.45	1.00	-0.76	-0.73	0.17	0.91	-0.10	0.21
MAE	-0.15	0.30	-0.51	-0.44	-0.44	-0.56	0.60	0.78	0.17	0.67	-0.53	0.15	-0.08	-0.44	-0.81	-0.76	1.00	1.00	0.18	-0.84	0.03	0.09
RMSE	-0.21	0.33	-0.51	-0.45	-0.42	-0.60	0.60	0.80	0.22	0.72	-0.57	0.20	-0.03	-0.47	-0.84	-0.73	1.00	1.00	0.24	-0.82	-0.03	0.08
ubRMSE	-0.84	0.57	0.02	0.00	0.03	-0.72	0.00	0.32	0.81	0.82	-0.57	0.70	0.53	-0.52	-0.58	0.17	0.18	0.24	1.00	0.13	-0.69	-0.04
R^2	-0.04	-0.06	0.43	0.39	0.26	0.16	-0.63	-0.81	0.35	-0.46	0.44	-0.10	0.06	0.30	0.66	0.91	-0.84	-0.82	0.13	1.00	0.03	0.36
R	0.58	-0.17	-0.12	0.19	-0.48	0.47	-0.33	-0.40	-0.28	-0.57	0.75	-0.59	-0.54	0.07	0.46	-0.10	0.03	-0.03	-0.69	0.03	1.00	0.62
KGE	0.25	0.27	0.04	0.17	-0.26	-0.27	-0.15	-0.46	0.50	-0.18	0.28	-0.23	-0.50	0.10	0.25	0.21	0.09	0.08	-0.04	0.36	0.62	1.00

Figure 5.2: Correlation matrix of the study variables' daily mean and standard deviation, and the daily evaluation metrics. The day of the year (Fieldtrip), L-band brightness temperature vertical (T_B^V) and horizontal (T_B^H), nadir angle (α), 12 cm soil moisture (HSII), NDVI, alfalfa height (Alfalfa), 12 cm soil temperature (T_G), days from last precipitation (Last Rain), days from last irrigation (Last irrigation) were spatially aggregated or assumed constant for each day.

5.2 Limitations & Recommendations

This study was performed under the assumptions of isotropic conditions and the homogeneous spatial distribution of scattering, soil and vegetation temperature, soil roughness, and dielectric properties. This study likewise assumed the nonlinear relationship between NDVI and VWC proposed by Chan et al. (2013). Nonetheless, Ye et al. (2024) demonstrates that a simple linear relationship can be used for sUAS operations, and these findings should be considered for future endeavors. Additionally, studies like Sanchez et al. (2014) demonstrate the utility of alternative vegetation indexes from hyperspectral imagery to obtain low-elevation sUAS water content retrievals. The methodology developed under this effort should include unique site calibrations when transposed to other regions of interest with different vegetation and soil conditions. Ground truth validation of vegetation water content with destructive methods is encouraged for future applications of this technology. Thermal infrared imagers should be included to capture the spatial variations in surface temperature when dealing with complex landscapes. The same principles proposed here could be extended to applications using lower frequency radiometers, such as the P-band radiometer used by Brakhasi et al. (2024), and modeling efforts such as Fluhrer et al. (2024) could be used to estimate deeper profiles. Nonetheless, L-band and P-band retrievals should suffice for root-zone soil moisture retrieval, even under higher conditions of vegetation water content.

Although the study did not extensively explore the effects of mission design on the Polarized L-band Radiometer's (PoLRa's) readings, it offered insights into the challenges associated with optimizing path design, flight speed, and inclination to suit this sensor. Additionally, it highlighted the limitations in spatial accuracy that need to be considered.

The one-second precision in synchronizing UAV navigation data with the radiometer's readings introduced a spatial uncertainty of 5.5 m under a cruise speed of 5.5 m/s (cruise speed for this study). This uncertainty can be mitigated by adjusting the elevation proportionally to the footprint, with the trade-off of coarser resolution. Alternatively, flying at a slower speed at a constant elevation can address the issue, albeit at the cost of increased flown distance. While treating the problem through single-angle or multi-angle modeling can yield diverse results, the PoLRa's fixed-angle installation introduced noise to the captured data. The accuracy of the time-matching process between drone Inertial Measurement Unit (IMU) data and the radiometer was a limiting factor when fast fluctuations occurred. Sudden angle changes (<1 second) caused by copter movement, wind, and direction changes generated challenging-to-track noise. Implementing a gimbal or fixing a constant inclination angle from the flight planner could significantly reduce noise due to uncontrolled angle changes. Direct communication between the payload and the drone may diminish uncertainties related to time matching. Again, reducing flight speed decreases the spatial uncertainty of microwave readings but comes at the expense of flight time, battery usage, and coverage. Electronically synchronizing the UAV and payload can potentially minimize the time difference, enhancing accuracy.

The generation of validation data for the drone is costly, as volumetric sampling required at least 5 minutes per sample, translating to around 4 hours to sample 49 points. This limitation hinders the extensive use of gravimetric samples for validation and calibration, making the calibration process resource-intensive regarding both probes and time. Despite the improvement in the sensor's surveying efficiency, achieving precise readings still demands substantial infrastructure resources for calibration. Due to the extensive demands in the calibration effort, this soil moisture modeling technology may perform best under high-yield crop conditions. Vegetation water content below 5 $\mathrm{kg/m^2}$ is recommended for traditional approaches(Das et al., 2019; Kerr et al., 2012), but recent promising estimations have been achieved with corn crops up to 22 $\mathrm{kg/m^2}$ by Brakhasi et al. (2024). Alternatively, this approach could benefit from already installed infrastructure such as water wheels, tractors, mowers, and cranes, and due to the passive emissions of the environment, it could also be applied to greenhouse operations. For outdoor applications, using sUAS dock platforms can reduce the need for a pilot or crew to optimize the efficiency of the retrievals.

Chapter 6

Conclusions

Despite the numerous studies employing microwave radiometry for soil moisture retrieval, the application of copter Unmanned Aerial Vehicle (UAV) operations for high-resolution retrievals still needs to be explored. This study presented an alternative approach to soil moisture surveying techniques, achieving state-of-the-art accuracy using airborne data from commercial platforms. This study employed the single soil moisture retrieval TO EM algorithm and estimated vegetation opacity through UAV multispectral imagery. Due to the model's robustness and the instrument's versatility, L-band brightness temperature can be modeled to retrieve soil moisture with single or dual polarization readings for 12 cm surface soil moisture retrieval while demanding substantial resources for calibration and validation. Vegetation opacity (τ) from UAV obtained NDVI provided a high resolution (6-8 cm GSD) source of mean vegetation water content that concurred with the observed vegetation cover. The retrieval of surface soil moisture was evaluated with an RMSE of 0.054 cm^3/cm^3 for moisture values within 0.08 and 0.42 cm^3/cm^3 over different stages of the alfalfa crop cycle with mean elevation and footprint area of 7m and 31.31 m^2, respectively. This study suggested the inclusion of ground truth vegetation water content validation, complimentary IR temperature surveying, a gimbal mount, and an electronic shutter inclusion for the Portable L-band radiometer (PoLRa). These modifications could reduce the uncertainties of the experiment and increase overall performance.

This endeavor highlighted the potential of commercial UAVs equipped with L-band radiometers and multispectral imagers to achieve state-of-the-art soil moisture retrievals in semi-arid lands and vegetation water content retrievals for low canopy croplands (and potentially grasslands, shrublands, or similar land covers).

Bibliography

Acevo-Herrera, R., Aguasca, A., Bosch-Lluis, X., & Camps, A. (2009). On the use of compact L-band Dicke radiometer (ARIEL) and UAV for soil moisture and salinity map retrieval: 2008/2009 field experiments [ISSN: 2153-7003]. *2009 IEEE International Geoscience and Remote Sensing Symposium*, *4*, IV–729–IV–732. https://doi.org/10.1109/IGARSS.2009.5417480

Acevo-Herrera, R., Aguasca, A., Bosch-Lluis, X., Camps, A., Martínez-Fernández, J., Sánchez-Martín, N., & Pérez-Gutiérrez, C. (2010). Design and First Results of an UAV-Borne L-Band Radiometer for Multiple Monitoring Purposes [Number: 7 Publisher: Molecular Diversity Preservation International]. *Remote Sensing*, *2*(7), 1662–1679. https://doi.org/10.3390/rs2071662

Bao, S., Wang, H., Zhang, R., Yan, H., & Chen, J. (2019). Comparison of Satellite-Derived Sea Surface Salinity Products from SMOS, Aquarius, and SMAP. *Journal of Geophysical Research: Oceans*, *124*(3), 1932–1944. https://doi.org/10.1029/2019JC014937

Brakhasi, F., Walker, J. P., Judge, J., Liu, P.-W., Shen, X., Ye, N., Wu, X., Yeo, I.-Y., Boopathi, N., Kim, E., Kerr, Y. H., & Jackson, T. J. (2024). A Comparison of Passive Microwave Emission Models for Estimating Brightness Temperature at L- and P-Bands Under Bare and Vegetated Soil Conditions [Conference Name: IEEE Journal of Selected Topics in Applied Earth Observations and Remote Sensing]. *IEEE Journal of Selected Topics in Applied Earth Observations and Remote Sensing*, *17*, 2570–2585. https://doi.org/10.1109/JSTARS.2023.3344764

Byrd, R. H., Lu, P., Nocedal, J., & Zhu, C. (1995). A Limited Memory Algorithm for Bound Constrained Optimization [Publisher: Society for Industrial and Applied Mathematics]. *SIAM Journal on Scientific Computing*, *16*(5), 1190–1208. https://doi.org/10.1137/0916069

Calla, O., Bohra, D., Vyas, R., Purohit, B. S., Prasher, R., Loomba, A., & Kumar, N. (2008). Measurement of soil moisture using microwave radiometer. *2008 International Conference on Recent Advances in Microwave Theory and Applications*, 621–624. https://doi.org/10.1109/AMTA.2008.4763147

Chan, S., Bindlish, R., Hunt, R., Jackson, & Kimball, J. (2013). Ancillary Data Report for Vegetation Water Content. Retrieved February 28, 2023, from https://smap.jpl.nasa.gov/system/internal_resources/details/original/289_047_veg_water.pdf

Chan, S., Njoku, E. G., & Colliander, A. (2012). Soil Moisture Active Passive (SMAP) Algorithm Theoretical Basis Document (ATBD). Retrieved January 19, 2023, from https://www.semanticscholar.org/paper/Soil-Moisture-Active-Passive-(SMAP)-Algorithm-Basis-Chan-Njoku/0acf97080b0aa53b04bd726bc172ce3972c52027 [TLDR] The ATBDs include a description of variance and uncertainty estimates and considerations of calibration and validation, exception control and diagnostics, and internal and external data flows are described.

Chen, F., Crow, W. T., Cosh, M. H., Colliander, A., Asanuma, J., Berg, A., Bosch, D. D., Caldwell, T. G., Collins, C. H., Jensen, K. H., Martínez-Fernández, J., Mcnairn, H., Starks, P. J., Su, Z., & Walker, J. P. (2019). Uncertainty of Reference Pixel Soil Moisture Averages Sampled at SMAP Core Validation Sites [Publisher: American Meteorological Society]. *Journal of Hydrometeorology*, *20*(8), 1553–1569. Retrieved April 11, 2024, from https://www.jstor.org/stable/26832261

Dai, E., Gasiewski, A., Stachura, M., & Elston, J. (2016). L-band Soil Moisture mapping using a suas for validation and calibration of SMAP [ISSN: 2153-7003]. *2016 IEEE International Geoscience and Remote Sensing Symposium (IGARSS)*, 3134–3136. https://doi.org/10.1109/IGARSS.2016.7729810

Dai, E., Gasiewski, A., Venkitasubramony, A., Stachura, M., & Elston, J. (2021). High Spatial Resolution Soil Moisture Mapping Using a Lobe Differencing Correlation Radiometer on a Small Unmanned Aerial System [Conference Name: IEEE Transactions on Geoscience and Remote Sensing]. *IEEE Transactions on Geoscience and Remote Sensing*, *59*(5), 4062–4079. https://doi.org/10.1109/TGRS.2020.3005385

Das, N. N., Entekhabi, D., Dunbar, R. S., Chaubell, M. J., Colliander, A., Yueh, S., Jagdhuber, T., Chen, F., Crow, W., O'Neill, P. E., Walker, J. P., Berg, A., Bosch, D. D., Caldwell, T., Cosh, M. H., Collins, C. H., Lopez-Baeza, E., & Thibeault, M. (2019). The SMAP and Copernicus Sentinel 1A/B microwave active-passive high resolution surface soil moisture product. *Remote Sensing of Environment*, *233*, 111380. https://doi.org/10.1016/j.rse.2019.111380

Entekhabi, D., Njoku, E. G., O'Neill, P. E., Kellogg, K. H., Crow, W. T., Edelstein, W. N., Entin, J. K., Goodman, S. D., Jackson, T. J., Johnson, J., Kimball, J., Piepmeier, J. R., Koster, R. D., Martin, N., McDonald, K. C., Moghaddam, M., Moran, S., Reichle, R., Shi, J. C., . . . Van Zyl, J. (2010). The Soil Moisture Active Passive (SMAP) Mission [Conference Name: Proceedings of the IEEE]. *Proceedings of the IEEE*, *98*(5), 704–716. https://doi.org/10.1109/JPROC.2010.2043918

Entekhabi, D., Reichle, R. H., Koster, R. D., & Crow, W. T. (2010). Performance Metrics for Soil Moisture Retrievals and Application Requirements. *Journal of Hydrometeorology*, *11*(3), 832–840. https://doi.org/10.1175/2010JHM1223.1

Fluhrer, A., Jagdhuber, T., Montzka, C., Schumacher, M., Alemohammad, H., Tabatabaeenejad, A., Kunstmann, H., & Entekhabi, D. (2024). Soil moisture profile estimation by combining P-band SAR polarimetry with hydrological and multi-layer scattering models. *Remote Sensing of Environment*, *305*, 114067. https://doi.org/10.1016/j.rse.2024.114067

Houtz, D., Matzler, C., Naderpour, R., Schwank, M., & Steffen, K. (2021). Quantifying Surface Melt and Liquid Water on the Greenland Ice Sheet using L-band Radiometry. *Remote Sensing of Environment*, *256*, 112341. https://doi.org/10.1016/j.rse.2021.112341

Houtz, D., Naderpour, R., & Schwank, M. (2020a). A Cost-Effective Portable L-Band Radiometer for Drone and Ground-Based Applications, 6531–6534. https://doi.org/10.1109/IGARSS39084.2020.9324231

Houtz, D., Naderpour, R., & Schwank, M. (2020b). Portable L-Band Radiometer (PoLRa): Design and Characterization. *Remote Sensing*, *12*. https://doi.org/10.3390/rs12172780

Iglhaut, J., Cabo, C., Puliti, S., Piermattei, L., O'Connor, J., & Rosette, J. (2019). Structure from Motion Photogrammetry in Forestry: A Review. *Current Forestry Reports*, *5*(3), 155–168. https://doi.org/10.1007/s40725-019-00094-3

Jackson, T. J., & Schmugge, T. J. (1991). Vegetation effects on the microwave emission of soils. *Remote Sensing of Environment*, *36*(3), 203–212. https://doi.org/10.1016/0034-4257(91)90057-D

Karthikeyan, L., Pan, M., Wanders, N., Kumar, D. N., & Wood, E. F. (2017a). Four decades of microwave satellite soil moisture observations: Part 1. A review of retrieval algorithms. *Advances in Water Resources*, *109*, 106–120. https://doi.org/10.1016/j.advwatres.2017.09.006

Karthikeyan, L., Pan, M., Wanders, N., Kumar, D. N., & Wood, E. F. (2017b). Four decades of microwave satellite soil moisture observations: Part 2. Product validation and inter-satellite comparisons. *Advances in Water Resources*, *109*, 236–252. https://doi.org/10.1016/j.advwatres.2017.09.010

Kerr, Y. H., & Njoku, E. G. (1990). A semiempirical model for interpreting microwave emission from semiarid land surfaces as seen from space [Conference Name: IEEE Transactions on Geoscience and Remote Sensing]. *IEEE Transactions on Geoscience and Remote Sensing*, *28*(3), 384–393. https://doi.org/10.1109/36.54364

Kerr, Y. H., Waldteufel, P., Richaume, P., Wigneron, J. P., Ferrazzoli, P., Mahmoodi, A., Al Bitar, A., Cabot, F., Gruhier, C., Juglea, S. E., Leroux, D., Mialon, A., & Delwart, S. (2012). The SMOS Soil Moisture Retrieval Algorithm [Conference Name: IEEE Transactions on Geoscience and Remote Sensing]. *IEEE Transactions* *on Geoscience and Remote Sensing*, *50*(5), 1384–1403. https://doi.org/10.1109/TGRS.2012.2184548

Konings, A. G., Piles, M., Rötzer, K., McColl, K. A., Chan, S. K., & Entekhabi, D. (2016). Vegetation optical depth and scattering albedo retrieval using time series of dual-polarized L-band radiometer observations. *Remote Sensing of Environment*, *172*, 178–189. https://doi.org/10.1016/j.rse.2015.11.009

Longuet-Higgins, H. C. (1981). A computer algorithm for reconstructing a scene from two projections. *Nature*, *293*, 133–135. https://doi.org/10.1038/293133a0

Matzler, C., & Murk, A. (2010). *Complex dielectric constant of dry sand in the 0.1 to 2 GHz range*. https://doi.org/10.13140/2.1.2387.9044

McIntyre, E., & Gasiewski, A. (2007). An ultra-lightweight L-band digital Lobe-Differencing Correlation Radiometer (LDCR) for airborne UAV SSS mapping [ISSN: 2153-7003]. *2007 IEEE International Geoscience and Remote Sensing Symposium*, 1095–1097. https://doi.org/10.1109/IGARSS.2007.4422992

Mo, T., Choudhury, B. J., Schmugge, T. J., Wang, J. R., & Jackson, T. J. (1982). A model for microwave emission from vegetation-covered fields [NTRS Author Affiliations: Computer Sciences Corp., NASA Goddard Space Flight Center, U.S. Department of Agriculture, Hydrology Laboratory, Beltsville NTRS Document ID: 19830039005 NTRS Research Center: Legacy CDMS (CDMS)]. *Journal of Geophysical Research*, *87*. Retrieved January 19, 2023, from https://ntrs.nasa.gov/citations/19830039005

Njoku, E. G., & Entekhabi, D. (1996). Passive microwave remote sensing of soil moisture. *Journal of Hydrology*, *184*(1), 101–129. https://doi.org/10.1016/0022-1694(95)02970-2

Özyeşil, O., Voroninski, V., Basri, R., & Singer, A. (2017). A survey of structure from motion*. [Publisher: Cambridge University Press]. *Acta Numerica*, *26*, 305–364. https://doi.org/10.1017/S096249291700006X

Panciera, R., Walker, J. P., Kalma, J. D., Kim, E. J., Saleh, K., & Wigneron, J.-P. (2009). Evaluation of the SMOS L-MEB passive microwave soil moisture retrieval algorithm.

Remote Sensing of Environment, *113*(2), 435–444. https://doi.org/10.1016/j.rse.2008.10.010

Park, C.-H., Jagdhuber, T., Colliander, A., Lee, J., Berg, A., Cosh, M., Kim, S.-B., Kim, Y., & Wulfmeyer, V. (2020). Parameterization of Vegetation Scattering Albedo in the Tau-Omega Model for Soil Moisture Retrieval on Croplands [Number: 18 Publisher: Multidisciplinary Digital Publishing Institute]. *Remote Sensing*, *12*(18), 2939. https://doi.org/10.3390/rs12182939

Sanchez, N., Piles, M., Martínez-Fernández, J., Vall-llossera, M., Pipia, L., Camps, A., Aguasca, A., Pérez Aragüés, F., & Herrero-Jiménez, C. (2014). Hyperspectral Optical, Thermal, and Microwave L-Band Observations For Soil Moisture Retrieval at Very High Spatial Resolution. *Photogrammetric Engineering and Remote Sensing*, *80*, 745–755. https://doi.org/10.14358/PERS.80.8.745

Schwank, M., Naderpour, R., & Mätzler, C. (2018). "Tau-Omega"- and Two-Stream Emission Models Used for Passive L-Band Retrievals: Application to Close-Range Measurements over a Forest [Number: 12 Publisher: Multidisciplinary Digital Publishing Institute]. *Remote Sensing*, *10*(12), 1868. https://doi.org/10.3390/rs10121868

Shen, X., Walker, J. P., Ye, N., Wu, X., Brakhasi, F., Boopathi, N., Zhu, L., Yeo, I.-Y., Kim, E., Kerr, Y., & Jackson, T. (2022). Evaluation of the tau-omega model over bare and wheat-covered flat and periodic soil surfaces at P- and L-band. *Remote Sensing of Environment*, *273*, 112960. https://doi.org/10.1016/j.rse.2022.112960

Srivastava, P. K. (2017). Satellite Soil Moisture: Review of Theory and Applications in Water Resources. *Water Resources Management*, *31*(10), 3161–3176. https://doi.org/10.1007/s11269-017-1722-6

Srivastava, P. K., O'Neill, P., Cosh, M., Kurum, M., Lang, R., & Joseph, A. (2015). Evaluation of Dielectric Mixing Models for Passive Microwave Soil Moisture Retrieval Using Data From ComRAD Ground-Based SMAP Simulator [Conference Name: IEEE Journal of Selected Topics in Applied Earth Observations and Remote Sensing]. *IEEE Journal of Selected Topics in Applied Earth Observations and Remote Sensing*, *8*(9), 4345–4354. https://doi.org/10.1109/JSTARS.2014.2372031

Susha, L., Singh, D. N., & Shojaei Baghini, M. (2014). A critical review of soil moisture measurement. *Measurement*, *54*, 92–105. https://doi.org/10.1016/j.measurement.2014.04.007

Topp, G. C., Davis, J. L., & Annan, A. P. (1980). Electromagnetic determination of soil water content: Measurements in coaxial transmission lines. *Water Resources Research*, *16*(3), 574–582. https://doi.org/10.1029/WR016i003p00574

Valencia, E., Acevo-Herrera, R., Bosch-Lluis, X., Aguasca, A., Rodriiguez-Alvarez, N., Ramos-Perez, I., Marchan-Hernandez, J., Glenat, M., Bou, F., & Camps, A. (2008). Initial Results of an Airborne Light-Weight L-Band Radiometer [ISSN: 2153-7003]. *IGARSS 2008 - 2008 IEEE International Geoscience and Remote Sensing Symposium*, *2*, II–1176–II–1179. https://doi.org/10.1109/IGARSS.2008.4779210

van de Griend, A., Owe, M., de Ruiter, J., & Gouweleeuw, B. (1996). Measurement and behavior of dual-polarization vegetation optical depth and single scattering albedo at 1.4- and 5-GHz microwave frequencies [Conference Name: IEEE Transactions on Geoscience and Remote Sensing]. *IEEE Transactions on Geoscience and Remote Sensing*, *34*(4), 957–965. https://doi.org/10.1109/36.508412

Wang, J. R., & Choudhury, B. J. (1981). Remote sensing of soil moisture content, over bare field at 1.4 GHz frequency. *Journal of Geophysical Research: Oceans*, *86*(C6), 5277–5282. https://doi.org/10.1029/JC086iC06p05277

Wigneron, J. .-., Kerr, Y., Waldteufel, P., Saleh, K., Escorihuela, M. .-., Richaume, P., Ferrazzoli, P., de Rosnay, P., Gurney, R., Calvet, J. .-., Grant, J. P., Guglielmetti, M., Hornbuckle, B., Mätzler, C., Pellarin, T., & Schwank, M. (2007). L-band Microwave Emission of the Biosphere (L-MEB) Model: Description and calibration against experimental data sets over crop fields. *Remote Sensing of Environment*, *107*(4), 639–655. https://doi.org/10.1016/j.rse.2006.10.014

Yayong, S., Jianwei, M., Jie, P., Shifeng, H., Kun, Y., Peng, Z., & He, Z. (2019). Preliminary Applicability Analysis of Soil Dielectric Constant Model of the Different Soil Texture Condition [ISSN: 2153-7003]. *IGARSS 2019 - 2019 IEEE International Geoscience and Remote Sensing Symposium*, 7148–7151. https://doi.org/10.1109/IGARSS.2019.8900240

Ye, N., Walker, J., Gao, Y., PopStefanija, I., & Hills, J. (2024). Comparison Between Thermal-Optical and L-Band Passive Microwave Soil Moisture Remote Sensing at Farm Scales: Towards UAV-Based Near-Surface Soil Moisture Mapping [Conference Name: IEEE Journal of Selected Topics in Applied Earth Observations and Remote Sensing]. *IEEE Journal of Selected Topics in Applied Earth Observations and Remote Sensing*, *17*, 633–642. https://doi.org/10.1109/JSTARS.2023.3329015

Zhu, C., Byrd, R. H., Lu, P., & Nocedal, J. (1997). Algorithm 778: L-BFGS-B: Fortran subroutines for large-scale bound-constrained optimization. *ACM Transactions on Mathematical Software*, *23*(4), 550–560. https://doi.org/10.1145/279232.279236

Appendix A

Appendix

Table A.1: Table of Algorithm Parameters by IGBP Class. Source: Chan et al., 2012.

ID	MODIS IGBP land classification	s	h	b	w	Stem factor
0	Water Bodies	-	0	0	0	–
1	Evergreen Needleleaf Forests	1.60	0.160	0.100	0.070	15.96
2	Evergreen Broadleaf Forests	1.60	0.160	0.100	0.070	19.15
3	Deciduous Needleleaf Forests	1.60	0.160	0.120	0.070	7.98
4	Deciduous Broadleaf Forests	1.60	0.160	0.120	0.070	12.77
5	Mixed Forests	1.60	0.160	0.110	0.070	12.77
6	Closed Shrublands	1.00	0.110	0.110	0.050	3.00
7	Open Shrublands	1.10	0.110	0.110	0.050	1.50
8	Woody Savannas	1.00	0.125	0.110	0.050	4.00
9	Savannas	1.00	0.156	0.110	0.080	3.00
10	Grasslands	1.56	0.156	0.130	0.050	1.50
11	Permanent Wetlands	1.00	0	0	0	4.00
12	Croplands Average	1.08	0.108	0.110	0.050	3.50
13	Urban and Built-up Lands	-	0	0.100	0.030	6.49
14	Crop-land/Natural Vegetation Mosaics	1.30	0.130	0.110	0.065	3.25
15	Snow and Ice	–	0	0	0	0
16	Barren	1.50	0.150	0	0	0

Table A.2: Stem factors for different MODIS IGBP land cover types. Source: (Chan et al., 2013).

IGBP	Land Cover	Stem Factor
1	Evergreen needleleaf forest	15.96
2	Evergreen broadleaf forest	19.15
3	Deciduous needleleaf forest	7.98
4	Deciduous broadleaf forest	12.77
5	Mixed forest	12.77
6	Closed shrublands	3.00
7	Open shrublands	1.50
8	Woody savannas	4.00
9	Savannas	3.00
10	Grasslands	1.50
11	Permanent wetlands	4.00
12	Croplands	3.50
13	Urban and built-up	6.49
14	Cropland/natural vegetation mosaic	3.25
15	Snow and ice	0.00
16	Barren or sparsely vegetated	0.00

Table A.3: Vegetation single scattering albedo ω provided by four independent scientific teams. The MDCA omega values were adopted after evaluation of the proposed omega values from the four independent teams [SMAP L2, SMAP L4, Multi-Temporal Dual Channel Algorithm (MT-DCA from MIT) and SMOS-IC].Source: Chan et al., 2012.

ID	MODIS IGBP land classification	SMAP SCA	SMAP L4	MTDCA	SMOS-IC	SMAP MDCA
0	Water Bodies	0	–	0	0	0
1	Evergreen Needleleaf Forests	0.050	0.11	0.07		0.07
2	Evergreen Broadleaf Forests	0.050	0.07	0.08	0.06	0.07
3	Deciduous Needleleaf Forests	0.050	0.11	0.06	0.06	0.07
4	Deciduous Broadleaf Forests	0.050	0.09	0.07	0.06	0.07
5	Mixed Forests	0.050	0.10	0.07	0.06	0.07
6	Closed Shrublands	0.050	0.09	0.08	0.10	0.08
7	Open Shrublands	0.050	0.09	0.06	0.08	0.07
8	Woody Savannas	0.050	0.12	0.08	0.06	0.08
9	Savannas	0.080	0.13	0.07	0.10	0.10
10	Grasslands	0.050	0.06	0.06	0.10	0.07
11	Permanent Wetlands	0	0.13	0.16	0.10	0.10
12	Croplands Average	0.050	0.10	0.10	0.12	0.06
13	Urban and Built-up Lands	0.030	0.10	0.08	0.10	0.08
14	Crop-land/ Natural Vegetation Mosaics	0.065	0.14	0.09	0.12	0.10
15	Snow and Ice	0	0.09	0.11	0.10	0.08
16	Barren	0	0.07	0.02	0.12	0.05

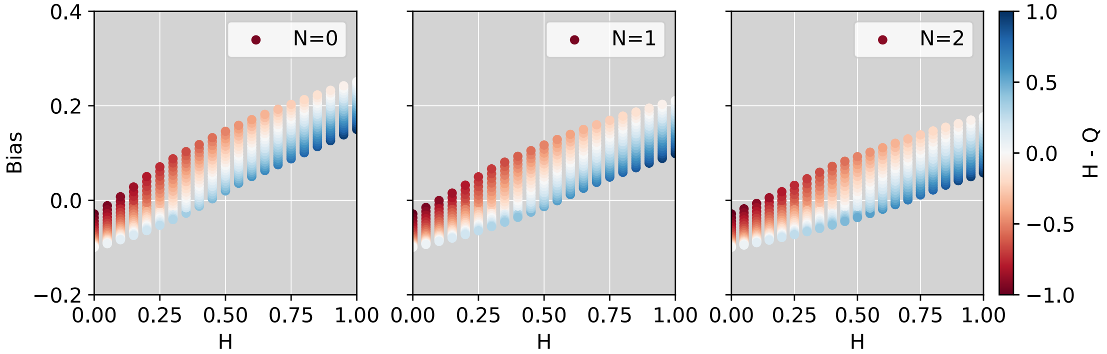

(a) Dual polarization.

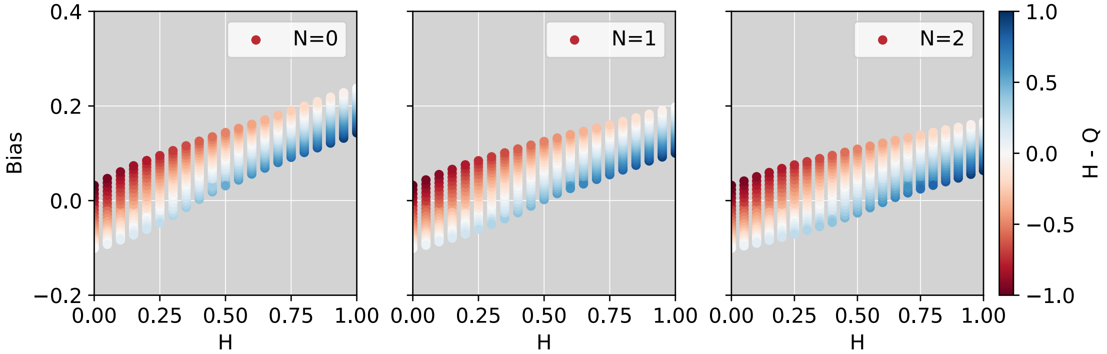

(b) Horizontal polarization.

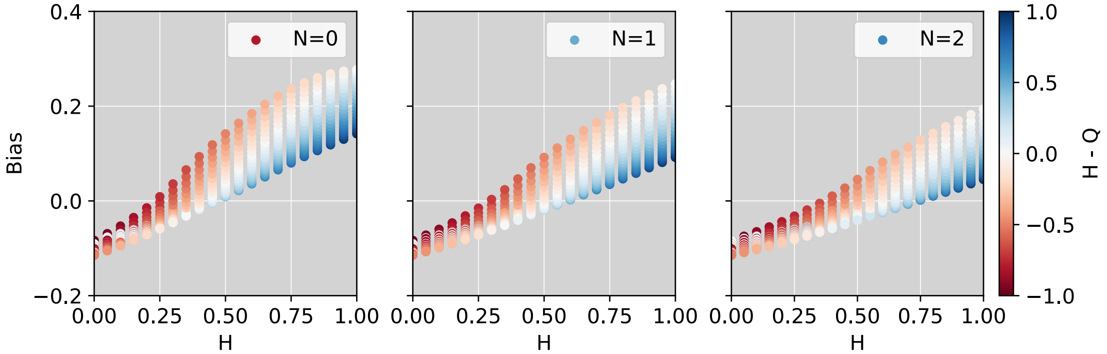

(c) Vertical polarization.

Figure A.1: H vs bias during the training phase for (a) dual polarization, (b) single horizontal and (c) vertical soil moisture retrievals with N = 0,1,2, colored by H−Q to distinguish trends for different relations between H and Q.

Curriculum Vitae

Santiago Hoyos Echeverri was born and raised in Medellín, Colombia. He developed his passion for sciences during his first years at Colegio Colombo Británico in Envigado, Antioquia. He graduated with an Environmental Engineering Bachelor from Universidad Nacional de Colombia at Medellín. While pursuing his bachelor's degree, he worked as an environmental management consultant in the tourism industry. After graduating, he worked as an environmental engineer intern for ISAGEN SAS for eight months. After finishing his contract, he joined The University of Texas at El Paso. He moved abroad to pursue his MS in Environmental Science while working as a Research Assistant at GeoSenSE in The Department of Earth, Environmental and Resource Sciences investigation in Hydrology, Remote Sensing, and Geospatial Sciences. Santiago obtained his Master of Science Degree in May 2024 after Defending his Thesis Titled Microwave Emission Model Parameter Tuning for Surface Soil Moisture Retrievals using UAV-mounted Dual Polarization L-band Radiometer. During his master's, Santiago taught Intro to GIS lab and trained multiple sUAS pilots at El Paso. Before graduation, Santiago joined The Systems Ecology Lab at The University of Texas at El Paso as a Geospatial Analyst. After graduation, he was offered a Research Associate position to join the lab's Arctic research and research support endeavors.

Contact Information:
shoyos20@outlook.com
https://www.linkedin.com/in/shoyose/